

University of Alberta

**Probing Molecular Interactions of Comb-type Polymers in
Air/Water/Solids Interfaces**

By

Ling Zhang

A thesis submitted to the Faculty of Graduate Studies and Research

in partial fulfillment of the requirements for the degree of

Master of Science

in

Chemical Engineering

Department of Chemical and Materials Engineering

©Ling Zhang

Fall 2012

Edmonton, Alberta

Permission is hereby granted to the University of Alberta Libraries to reproduce single copies of this thesis and to lend or sell such copies for private, scholarly or scientific research purposes only. Where the thesis is converted to, or otherwise made available in digital form, the University of Alberta will advise potential users of the thesis of these terms.

The author reserves all other publication and other rights in association with the copyright in the thesis and, except as herein before provided, neither the thesis nor any substantial portion thereof may be printed or otherwise reproduced in any material form whatsoever without the author's prior written permission.

ABSTRACT

Over the past decade, comb-type copolymers have attracted much attention in polymer chemistry and physics, nanotechnology, bioengineering and industrial applications. Using a surface forces apparatus (SFA), the molecular and surface interactions of two different kinds of comb-type polymers, polystyrene-graft-polyethylene oxide (PS-g-PEO) and polycarboxylate ether (PCE), were investigated under different solution conditions. Long-range repulsive forces were measured between PS-g-PEO films which were due to the steric hindrance between swollen PEO brushes and could be well described by the Alexander–de Gennes (AdG) scaling theory. Molecular forces and rheology study of PCE-kaolinite suspension showed that PCE molecules could induce bridging forces between kaolinite surfaces at low polymer concentration while lead to steric repulsion at high concentration, affected by solution conditions (e.g., pH). The results provide important insights into fundamental understanding of molecular interaction mechanisms of comb-type polymers at air/water/solids interfaces and the development of novel functional polymers/coatings for engineering and biomedical applications.

ACKNOWLEDGEMENT

I would like to express my sincere gratitude to Professor Hongbo Zeng and Professor Qingxia (Chad) Liu, for their valuable suggestions, help as well as encouragement during my MSc Study. Without their help and strong support, I could not complete the M.Sc. program so quickly and smoothly.

It was Dr. Zeng, my supervisor, who guided me into the research field of surface science and intermolecular forces of polymers which is now I am so interested in. Every time I discussed the research work with Dr. Zeng, the most important thing I learned is the way how he thinks about questions as well as his enthusiasm towards the research work. Besides that, he also gave me opportunities to be involved in other research fields which helped me gain more and were also beneficial for my further study.

Dr. Liu is a very experienced and knowledgeable professor from whom I learnt the attitude to the scientific research. We need critical thinking, an open mind, creativity and team work. He can always take time out from his busy schedule to meet every student in the group and also give us inspirations in the research work.

I am also very grateful to the postdoctoral fellow in the group, Qingye Lu, for her great patience and help with operating the surface forces apparatus (SFA). Many thanks to other members in my group including Ali Faghihnejad, Yaguan Ji and also thanks Jie Ru, Shengqun Wang in Dr. Xu's group, for their kind help and training me on some instruments.

I want to also thank my best friend here Jing Deng for her accompany no matter what happened and I also really appreciate my friend Xinwei Cui, who gave me guidance both in the research and life, and could also always stand by my side and support me.

I would like to thank my father, mother and my twin brother. Without their support and encouragement, I would never be able to live a good life here and to make my M.Sc. studies so smooth.

TABLE OF CONTENTS

CHAPTER 1	INTRODUCTION.....	1
1.1	Comb-type polymers.....	1
1.1.1	<i>Conformations of comb-type polymers</i>	1
1.1.2	<i>Review of previous work on comb-type polymers</i>	3
1.2	Intermolecular and surface forces	4
1.2.1	<i>van de Waals force</i>	4
1.2.2	<i>Electrostatic double layer force</i>	5
1.2.3	<i>Steric repulsion and bridging force</i>	7
	References.....	9
CHAPTER 2	EXPERIMENTAL TECHNIQUES	11
2.1	The surface forces apparatus (SFA).....	11
2.2	Multiple beam interferometry (MBI).....	15
2.3	Mica sheets preparation	17
2.4	Normal force measurement.....	19
2.5	Adhesion measurement using SFA (contact mechanics — JKR theory)	
	21	
2.6	Other techniques	22
2.7	X-ray Photoelectron Spectroscopy (XPS)	25
	References.....	27

CHAPTER 3	PROBING MOLECULAR AND SURFACE	
INTERACTIONS OF COMB-TYPE POLYMER POLYSTYRENE-GRAFT-	POLYETHYLENE OXIDE (PS-G-PEO).....	29
3.1	Introduction.....	29
3.2	Materials and Experimental Methods	31
3.2.1	<i>Materials and samples preparation</i>	<i>31</i>
3.2.2	<i>Surface force measurement in aqueous solution using SFA.....</i>	<i>33</i>
3.2.3	<i>Adhesion measurement (contact mechanics) in air using SFA.....</i>	<i>35</i>
3.2.4	<i>Contact angle measurement.....</i>	<i>36</i>
3.2.5	<i>AFM imaging</i>	<i>36</i>
3.2.6	<i>X-ray photoelectron spectroscopy (XPS).....</i>	<i>37</i>
3.3	Results and Discussion	38
3.3.1	<i>Characterization of PS-g-PEO polymer film.....</i>	<i>38</i>
3.3.2	<i>Interaction forces between PS-g-PEO films in NaCl solution.....</i>	<i>42</i>
3.4	Surface energy of PS-g-PEO film.....	50
3.4.1	<i>Contact mechanics test</i>	<i>50</i>
3.4.2	<i>Surface energy by three-probe-liquid contact angle measurement ..</i>	<i>54</i>
3.5	Conclusion	57
	Acknowledgement	58
	Supplementary Information	59
	<i>X-ray photoelectron spectroscopy (XPS).....</i>	<i>59</i>
	<i>Alexander de Gennes (AdG) fitting of force-distance profiles using single set</i>	<i>60</i>
	

of parameters.....	60
References.....	62
CHAPTER 4 EFFECT OF POLYCARBOXYLATE ETHER COMB- TYPE POLYMER ON VISCOSITY AND INTERFACIAL PROPERTIES OF KAOLINITE CLAY SUSPENSION	67
4.1 Introduction.....	67
4.2 Materials	69
4.3 Experimental Methods	70
4.3.1 <i>Sample preparation</i>	70
4.3.2 <i>Viscosity measurement</i>	71
4.3.3 <i>Zeta potential measurement</i>	71
4.3.4 <i>Settling tests</i>	72
4.3.5 <i>Measurement of interaction force using Surface Forces Apparatus</i>	72
4.4 Results and discussion	73
4.4.1 <i>Impact of pH on viscosity of kaolinite suspensions</i>	73
4.4.2 <i>Effect of PCE on viscosity of kaolinite suspension</i>	75
4.4.3 <i>Settling tests</i>	84
4.4.4 <i>Interactions between kaolinite clay particles and PCE polymer</i>	87
4.5 Conclusion	97
Supplementary Information	99
<i>Effects of solid content</i>	99
References.....	101
CHAPTER 5 SUMMARY	105

References 108

LIST OF TABLES

Table 3.1 Fitting parameters using the Alexander-de Gennes Theory for experimentally measured force-distance profiles at both high and low compression regimes in Figure 3.6.	50
Table 3.2 Three probe liquids for measuring the surface energy of PS-g-PEO film.	56
Table 3.3 The contact angles of three probe liquids on PS-g-PEO film.	56
Table 3.4 The surface energy of PS-g-PEO film.	56
Table 4.1 Power law exponents m in $\eta \propto \dot{\gamma}^m$ for kaolinite suspensions with different PCE dosages at pH=3.4 and 8.3.	79

LISTS OF FIGURES

Figure 1.1 Comb-type polymers with flexible (a) homopolymer graft chains, (b) copolymer graft chains, (c) hetero-graft chains, and (d) branched graft chains.	2
Figure 1.2 Schematic of double layer structure on a negatively charged surface in a liquid.	7
Figure 2.1 Schematic drawing of SFA 2000.....	12
Figure 2.2 Schematic drawing of a typical SFA experimental setup.....	14
Figure 2.3 FECO fringes in a typical force measurement (two mica surfaces in adhesive contact).....	15
Figure 2.4 Schematic of FECO fringes to measure the radius of local curvature of two surfaces.	17
Figure 2.5 The schematic drawing of mica sheets preparation procedure: (a) trimming, (b) splitting, (c) peeling, (d) cutting and (e) silvering.....	19
Figure 2.6 Schematic of the principle of normal force measurement.....	20
Figure 2.7 Schematic drawing of AFM working principle.....	24
Figure 2.8 Illustration of contact angle of a liquid on a solid surface.....	25
Figure 2.9 A brief schematic of photoelectron emission process	26
Figure 3.1 Chemical structure of comb-type polymer PS-g-PEO used in this study.	33
Figure 3.2 Experimental configurations of surface forces measurement: (a) PS-g-PEO film coated on mica surface versus a bare mica surface in NaCl solution (asymmetric case), (b) two PS-g-PEO films coated on two mica	

surfaces in NaCl solution (symmetric case), (c) schematic of two polymer surfaces in adhesive contact in air and typical FECO fringes. 34

Figure 3.3 The AFM images of PS-g-PEO film (a) before treatment, (b) after water treatment. 40

Figure 3.4 Contact angle of water on spin-coated PS-g-PEO film. 42

Figure 3.5 Force-distance profiles between a PS-g-PEO polymer film and a bare mica surface (asymmetric configuration) and between two PS-g-PEO polymer films (symmetric configuration) in aqueous solution of (a) 1 mM NaCl (b) 100 mM NaCl..... 43

Figure 3.6 Experimentally measured force-distance profiles (dot plots) for PS-g-PEO vs mica (asymmetric configuration) and two PS-g-PEO surfaces (symmetric configuration) and theoretically fitted curves using the Alexander-de Gennes (AdG) theory in (a) 1 mM NaCl and (b) 100 mM NaCl solution. (c) Illustration of swollen PEO branches in water from polymer-water interface and sublayers in the polymer film. 49

Figure 3.7 Contact diameter $2r$ vs. applied load F_{\perp} obtained through the JKR loading-unloading test for two PS-g-PEO films. Red solid line is the fitted curve for the loading path using the JKR model. 54

Figure S3.1 High resolution XPS spectrum of spin-coated PS-g-PEO film: (a) C1s spectrum and (b) O1s spectrum. 59

Figure S3.2 Experimentally measured force-distance profiles (dot plots) for PS-g-PEO vs mica (asymmetric configuration) and two PS-g-PEO surfaces (symmetric configuration), and theoretically fitted curves using the AdG theory (using single

set of fitting parameters) in (a) 1 mM NaCl and (b) 100 mM NaCl solution.

61

Figure 4.1 (a) Chemical structure and (b) schematic structure (brush conformation) of a super-plasticizer, PCE used in this work 70

Figure 4.2 Impact of pH on the viscosity of 35 wt% kaolinite suspension. The inset is an expanded drawing of viscosity curve at pH=8.3..... 73

Figure 4.3 Effect of different PCE dosages on the viscosity of 35 wt% kaolinite suspension. Variation of viscosity as a function of shear rate at (a, c) pH=3.4 and (b, d) pH=8.3 in linear plots (a, b) and log-log plots (c, d). The viscosity changes of 35 wt% kaolinite suspension with different PCE dosages at shear rate 10 s^{-1} at (e) pH=3.4 and (f) pH=8.3..... 78

Figure 4.4 The square root of shear stress as a function of square root of shear rate at (a) pH=3.4 and (b) pH=8.3. The yield stress of 35wt% kaolinite suspension with different PCE dosages at (c) pH=3.4 and (d) pH=8.3. 82

Figure 4.5 The normalized increase of the viscosity of 35 wt% kaolinite suspension with 0.27 wt% of PCE dosage at pH=3.4 and pH=8.3..... 83

Figure 4.6 The impact of different PCE dosages on the pH of 35wt% kaolinite suspension..... 84

Figure 4.7 (a) The normalized height of mud line as a function of settling time with different PCE dosages; (b) the initial settling rate as a function of PCE dosages at pH=3.4 and 8.3 (Note: a volume settling rate of 1 ml/s corresponds to 1.8 mm/s for the 100 ml-graduated cylinders used here). 86

Figure 4.8 Real-time pictures for the settling of 2 wt% kaolinite suspensions at pH=3.4 for t=0, 2 and 5 minutes. Note: samples 1, 2 and 3 contain 0, 0.05 wt% and 0.40 wt% of PCE respectively	87
Figure 4.9 Microscope images of 2 wt% kaolinite suspension in the absence and presence of PCE (0.03 wt%) at pH=3.4 (a) and (b), and at pH=8.3 (c) and (d).....	90
Figure 4.10 Zeta potential of 2 wt% kaolinite suspension with different PCE dosages.....	91
Figure 4.11 Force-distance profiles between two mica surfaces in different concentrations of PCE solution both at pH=3.4 (a) and pH=8.3 (b). Open symbols represent approach and filled symbols represent separation. ..	92
Figure 4.12 Illustrations on the interactions between kaolinite particles and PCE molecules at acidic condition (pH=3.4) (a) & (b), and at alkaline condition (pH=8.3) (c) & (d): (a) pH=3.4 with low PCE dosage; (b) pH=3.4 with high PCE dosage; (c) pH=8.3 with low PCE dosage; (d) pH=8.3 with high PCE dosage.....	97
Figure S4.1 Effect of different PCE dosages on the viscosity of 10 wt% and 2 wt% kaolinite suspension at pH=8.3.....	100

SYMBOLS AND NOMENCLATURE

A	Hamaker constant, J
D	separation distance between surfaces, m
D_{jump}	distance one surface jump apart from the other surface, m
$D_{applied}$	the distance to move the surfaces at the base of the double-cantilever force springs, m
D_{actual}	the actual distance that the surfaces move relative to each other, m
R_1, R_2	radius of spherical particles, m
$\lambda_n^0, \lambda_{n-1}^0$	wavelength move of the nth and (n-1)th fringe, m
$\varphi(D)$	electrical potential, V
φ_0	surface potential of a particle, V
κ	inverse Debye length, m^{-1}
R_g	radius of gyration, m
l	length of the repeating unit in the polymer, m
N	number of repeating units in the polymer
Γ	surface coverage of polymer on the surface, m^{-2}
s	mean distance between the attachment points of adsorbed polymer chains, m

K_s	spring constant, N/m
$F_{adhesion}, F_{ad}$	adhesion force, N
γ	surface energy, mJ/m ²
γ_A	surface energy in the loading (advancing) process, mJ/m ²
γ_R	surface energy in the unloading (receding) process, mJ/m ²
$\Delta\gamma$	the hysteresis of surface energy, mJ/m ²
γ_{eff}	effective surface energy, mJ/m ²
γ_{SG}	surface energy at solid and gas interface, mJ/m ²
γ_{SL}	surface energy at solid and liquid interface, mJ/m ²
γ_{LG}	surface energy at liquid and gas interface, mJ/m ²
γ^d	the dispersive component (Lifshitz-Van der Waals interactions), mJ/m ²
γ^+, γ^-	the polar components (Lewis acid-base), mJ/m ²
r	radius of contact area, m
F_{\perp}	applied load normally to the surface, N
R	radius of the cylindrical silica disc, m
K	elastic moduli, N/m ²
η	apparent viscosity, Pa.s

$\dot{\gamma}$	shear rate, s^{-1}
τ	shear stress, Pa
τ_c	Casson yield stress, Pa
η_c	Casson viscosity, Pa.s
ω	angular velocity, rad/s
T	the torque, Nm
$h\nu$	X-ray photon energy, eV
E_b	binding energy, eV
E_k	kinetic energy of photoelectron, eV
$P(D)$	repulsive pressure between two surfaces, Pa
T	temperature, C°
L	brush layer thickness, m
k	Boltzmann constant, $1.381 \times 10^{-23} \text{ J K}^{-1}$
E_1, E_2	Young's moduli, N/m^2
ν_1, ν_2	Poisson's ratios
W, W_{ad}	adhesion energy, mJ/m^2

CHAPTER 1 INTRODUCTION

1.1 Comb-type polymers

Functionalities of polymer coatings play important roles in numerous engineering and biomedical applications, ranging from adhesion, lubrication, wettability control, drug delivery, stabilization/destabilization of colloids to antifouling treatments. During the past decade, comb-type polymers have attracted much attention in polymer chemistry and physics, nanotechnology and bioengineering, which are special copolymers with many branches grafted to a polymer backbone. Since only limited work is available on the molecular forces of comb-type polymers, this thesis work will provide some insights into the fundamental understanding of their molecular interaction mechanisms and designing and developing novel polymers and polymer coatings with engineering and biomedical applications.

1.1.1 Conformations of comb-type polymers

There are many kinds of comb-type polymers with different chemical structures in backbones and graft chains. Both backbone and graft chains can be flexible or stiff and the graft chains can be also homopolymers or copolymers [1, 2]. Figure 0.1 shows some typical structures of comb-type polymers with flexible graft chains. For comb-type polymers with the same chemical composition in backbone and graft chains, the polymer conformation can be controlled by varying the density and length of side chains as well as the solvent environment. Comb-type polymers with much denser side chains normally induce stronger

intramolecular steric interactions resulting in stretched backbones. Varying solution pH can make certain comb-type polymers either negatively or positively charged, leading to fully stretched conformation due to the intramolecular electrostatic repulsive forces. The solvent conditions (i.e. good solvent, bad solvent and theta (θ) solvent) also show strong impact on the polymer conformations [3]. In a good solvent, the favourable interactions between solvent molecules and polymer chains cause the polymers to expand. In a bad solvent, the interactions between polymer molecules are more favoured so that it leads the polymer molecules to coil. The theta (θ) solvent is also called ideal solvent in which the polymer acts as an ideal chain which can be modelled by using the free jointed chain model.

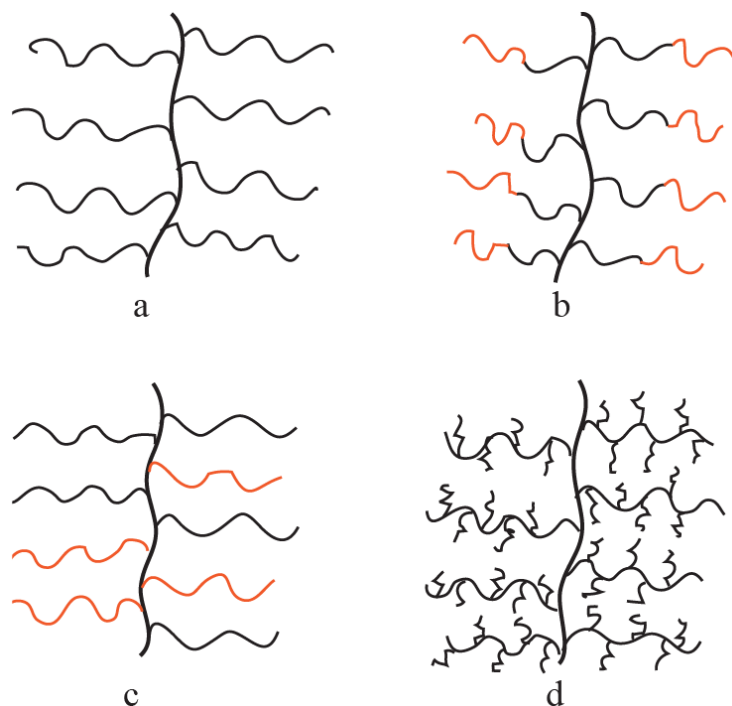


Figure 0.1 Comb-type polymers with flexible (a) homopolymer graft chains, (b) copolymer graft chains, (c) hetero-graft chains, and (d) branched graft chains.

1.1.2 Review of previous work on comb-type polymers

Comb-type polymers, with their special and interesting architecture, have attracted much attention in the fields of polymer chemistry and physics, nanotechnology, bioengineering and industrial applications. During the past two decades, much work has been focused on the synthesis and characterization of well-defined comb-type polymers using different synthesis methods and experimental techniques including gel permeation chromatography (GPC), light scattering (LS), viscosity measurement, atomic force microscopy (AFM), surface sensitive sum-frequency generation (SFG), etc. [1, 2, 4-8] Since the comb-type polymer may form brush conformation at the solid/water/air interfaces, some experimental work was reported on the adsorption behaviour and conformation of comb-type polymers, [6-8] and some other work focused on the theoretical modelling [9, 10]. Comb-type polycarboxylate ether (PCE) has been reported to be effective additives in stabilizing different colloidal systems by using viscosity measurement, isotherm adsorption, zeta potential measurement, etc. [7, 11-15] Normally, the backbone of the comb-type polymer can act as the adsorbing chain and graft side chains can extend from the surfaces performing as polymer brushes. Comb-type polymers, such as poly(L-lysine)-g-poly(ethylene glycol), poly(ethylenimine)-graft-poly(ethylene glycol) and polyacrylonitrile-graft-poly(ethylene oxide), have also been investigated in terms of the properties for applications of lubricants or anti-fouling coatings in bioengineering [16, 17].

1.2 Intermolecular and surface forces

The main objective of this study is to probe the molecular forces of comb-type polymers at water/solid/air interfaces to provide some fundamental insights into the design and development of functional and novel polymers with important industrial applications ranging from adhesives, lubricants, dispersants to anti-fouling materials. In this section, I describe the surface and intermolecular forces involved in this study including van de Waals forces, electrostatic force, polymer bridging force and steric repulsive force.

1.2.1 van de Waals force

The van de Waals force (VDW), named after the Dutch scientist Johannes Diderik van der Waals, is defined as the sum of attractive or repulsive force between molecules (dipoles) or between parts of the same molecules [18]. Van der Waals force includes three kinds of contributions: dipole-dipole interactions (Keesom force), dipole-induced dipole interactions (Debye force) and instantaneous induced dipole-induced dipole interactions (London dispersion force). Van de Waals force is considered to generally exist on all surfaces, but it is relatively weak compared to other forces due to covalent bonds or electrostatic interactions between ions, which decays quickly with increasing distance (D) between surfaces. For example, van de Waals force between two atoms is proportional to $-D^{-7}$. The van de Waals interactions also depend on the geometries of interacting surfaces. For examples, the VDW force between two flat surfaces is given by $F(D) = -A / 6\pi D^3$, and for two spherical particles, it is $F(D) = -AR_1R_2 / 6(R_1 + R_2)D^2$, where R_1 and R_2 are the radius of two spherical particles. A is the Hamaker constant which is

dependent on the chemical nature of interacting molecules or surfaces and defined as $A = \pi^2 C \rho_1 \rho_2$, where C is the coefficient in the atom-atom pair potential, ρ_1 and ρ_2 are the number of atoms per volume in the two bodies.

1.2.2 Electrostatic double layer force

The electrical double layer is a structure forming on a surface of an object (solid, air bubble, liquid drop) when it is placed in an aqueous surrounding. The double layer refers to the two layers near the surface. A typical schematic of double layer structure on a negatively charged surface in an aqueous solution is shown in Figure 0.2. [19] The first layer is called stern layer (i.e. Helmholtz layer) where the counter ions adsorb on the surface that is immobile. The second layer next to the first layer is called the diffuse layer or Gouy-Chapman layer. The diffuse layer consists of mobile ions that normally obey Poisson-Boltzmann statistics and associated with the surface via Coulomb force. The potential at the point or plane between the Stern layer and diffuse layer is called the zeta potential.

In the diffuse layer (the right side from the stern layer), the electrical potential decays exponentially following the equation (between two flat surface), $\varphi(D) = \varphi_0 \exp(-\kappa D)$. κ^{-1} is called Debye length and also considered as the double layer thickness. Therefore, when the two surfaces approach each other, the diffuse layers become overlapped and the repulsive force is induced, called electrostatic double layer force. The electrostatic double layer force is essential for the stabilization of many colloidal dispersions and polymer systems such as polyelectrolytes.

When an electric field is applied across an electrolyte solution, the viscous forces acting on the charged particles in the suspension tend to oppose the particles' movement towards the electrode with opposite charges. When these two opposing forces reach equilibrium, the movement of the particles in suspension will exhibit a constant velocity, which is commonly referred to as its electrophoretic mobility. Based on this model, the zeta potential of the particles can be described by the Smoluchowski equation as shown in Eq. 1.1. ,

$$\mu_E = \frac{2\varepsilon\zeta f(ka)}{3\eta} \quad (1.1)$$

where μ_E is electrophoretic mobility, ε is dielectric constant, ζ is zeta potential and η is viscosity of suspension. $f(ka)$ is so-called Henry's function and a is the particle radius. Two values are generally used as approximations for the $f(ka)$ determination, either 1.5 or 1.0. $f(ka)=1.5$ is referred to as the Smoluchowski approximation, which is normally applied to particles larger than about 0.2 microns. $f(ka)=1.0$ is commonly used for small particles in low dielectric constant media (e.g., non-aqueous measurements), referred to as the Huckel approximation.

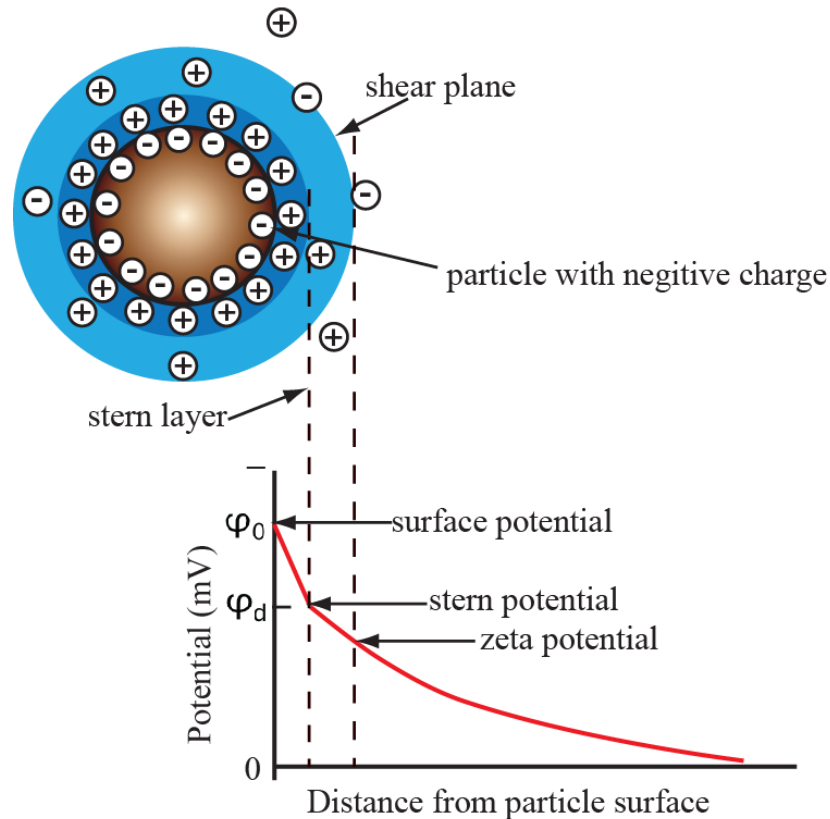


Figure 0.2 Schematic of double layer structure on a negatively charged surface in a liquid.

1.2.3 Steric repulsion and bridging force

In my study, the steric and bridging forces occurred between two surfaces bearing polymers or between two surfaces in the medium of polymer solution. When two surfaces covered with polymers opposing to each other, the net interactions include the polymer-polymer and polymer-surface interactions. Normally, the polymer-polymer interaction results in repulsive force referred as steric repulsive force and polymer-surface interaction can either lead to repulsive force or attractive force (bridging force). The conformation of a polymer depends on the condition of its surroundings, such as solvent quality, temperature, etc. [3]

If a polymer is in an ideal state which means the movement of the polymer cannot be affected by the monomer-monomer interactions, the dimension of the polymer molecule can be defined by the radius of gyration (R_g),

$$R_g = \frac{l\sqrt{N}}{\sqrt{6}} \quad (1.2)$$

where l is the length of the repeating unit and N is the number of repeating units in the polymer. There are two regimes of the polymer conformations which are dependent on the surface coverage of the polymer on the surfaces. The surface coverage Γ is the number of polymer chains adsorbing on the surface per unit area and the relation with the mean distance s between the two anchoring points of adsorbed polymer chains is shown in Eq. 1.3.

$$\Gamma = \frac{1}{s^2} \quad (1.3)$$

When the surface coverage is lower ($s > R_g$) and covered with a number of separated polymer blobs with height and size given by R_g which do not overlap, the polymer chains are in a regime called mushroom regime. Under high surface coverage ($s \ll R_g$), the polymers are in a so-called brush regime, whose surface interactions can be normally described by the Alexander de Gennes theory. [18, 20-22] In these two regimes, the steric repulsive interaction energy can be described by different equations or models [22]. However, the attractive component (or so-called bridging force) has no simple expression because the bridging force depends on the type of interactions (i.e., specific or non-specific) between the polymer and the opposite surface.

References

- [1] S.S. Sheiko, B.S. Sumerlin, K. Matyjaszewski, *Prog Polym Sci*, 33 (2008) 759.
- [2] M.F. Zhang, A.H.E. Muller, *J Polym Sci Pol Chem*, 43 (2005) 3461.
- [3] M.M. Coleman, *Fundamentals of Polymer Science: An Introductory Text*, Second Edition, CRC Press, 1998.
- [4] K. Ito, Y. Tomi, S. Kawaguchi, *Macromolecules*, 25 (1992) 1534.
- [5] M. Wintermantel, M. Schmidt, Y. Tsukahara, K. Kajiwara, S. Kohjiya, *Macromol Rapid Comm*, 15 (1994) 279.
- [6] M. Lesti, S. Ng, J. Plank, *J Am Ceram Soc*, 93 (2010) 3493.
- [7] Q.P. Ran, P. Somasundaran, C.W. Miao, J.P. Liu, S.S. Wu, J. Shen, *J Disper Sci Technol*, 31 (2010) 790.
- [8] K.S. Gautam, A. Dhinojwala, *Macromolecules*, 34 (2001) 1137.
- [9] A. Sartori, A. Johner, J.L. Viovy, J.F. Joanny, *Macromolecules*, 38 (2005) 3432.
- [10] I.I. Potemkin, *Macromolecules*, 39 (2006) 7178.
- [11] C.P. Whitby, P.J. Scales, F. Grieser, T.W. Healy, G. Kirby, J.A. Lewis, C.F. Zukoski, *J Colloid Interf Sci*, 262 (2003) 274.
- [12] A. Zingg, F. Winnefeld, L. Holzer, J. Pakusch, S. Becker, R. Figi, L. Gauckler, *Cement Concrete Comp*, 31 (2009) 153.

- [13] H. Hommer, *J Eur Ceram Soc*, 29 (2009) 1847.
- [14] J. Plank, C. Schroefl, M. Gruber, M. Lesti, R. Sieber, *J Adv Concr Technol*, 7 (2009) 5.
- [15] Q.P. Ran, P. Somasundaran, C.W. Miao, J.P. Liu, S.S. Wu, J. Shen, *J Colloid Interf Sci*, 336 (2009) 624.
- [16] S. Lee, M. Muller, M. Ratoi-Salagean, J. Voros, S. Pasche, S.M. De Paul, H.A. Spikes, M. Textor, N.D. Spencer, *Tribol Lett*, 15 (2003) 231.
- [17] M.A. Brady, F.T. Limpoco, S.S. Perry, *Langmuir*, 25 (2009) 744.
- [18] J. Israelachvili, *Intermolecular and Surface Forces*, third ed., Academic Press, 2011.
- [19] D. Myers, *Surfaces, Interfaces, and Colloids: Principles and Applications*, 2nd edition ed., John Wiley & Sons, Inc, New York, 1999.
- [20] M. Akbulut, A.R.G. Alig, Y. Min, N. Belman, M. Reynolds, Y. Golan, J. Israelachvili, *Langmuir*, 23 (2007) 3961.
- [21] P.G. Degennes, *Adv Colloid Interfac*, 27 (1987) 189.
- [22] F. Li, F. Pincet, *Langmuir*, 23 (2007) 12541.

CHAPTER 2 EXPERIMENTAL TECHNIQUES

1.3 The surface forces apparatus (SFA)

Surface forces apparatus (SFA) has been used for several decades to directly measure the intermolecular forces between surfaces. Since the first apparatus was described by Tabor, Winterton and Israelachvili in 1969 [1, 2], SFA has been being significantly developed and improved. [3-6]

After the development of early versions of SFA which can only measure the forces between surfaces in air or vacuum, the SFA Mk I was described by Israelachvili and Adam which allows the force measurement both in controlled vapors and liquids [3]. The travelling distance of mica surface controlled by the motor-driven micrometer and piezoelectric crystals was improved from micrometer to the angstrom level. In 1987, Israelachvili described the SFA Mk II as an improved version of the Mk I which allowed the upper surface to be moved in the lateral direction. Therefore, frictional forces can be also measured by using an SFA. The force sensitivity reached to <10 nN, which is the same with that of normal force measurement [7, 8].

In order to make SFA be used in much more complex systems, the Mk III, developed by Israelachvili and McGuiggan (1985-1989), was much more compact than the previous versions and also better for systems where the surfaces needed to be completely immersed in liquids. Moreover, a new attachment so-called bimorph slider was developed for the friction force measurement [5, 9].

Although the SFA Mk III is already very functional and stable, there are still some limitations. SFA 2000 is designed to have fewer parts and much more user friendly and also much easier to produce; at the same time, it still retains the good performance as the previous versions. A schematic of the main chamber of the basic SFA 2000 is shown in Figure 0.1 [6]. The main components are micrometers, main stage containing the central single-cantilever spring, lower disk holder and upper disk holder. There are totally four different controls to manipulate the separation distance between the two surfaces. The lower surface can be controlled by a differential micrometer and can be moved over a range of 2 mm with a position accuracy of 2 \AA . The upper surface can be moved by a piezoelectric crystal over a range of 1000 \AA with a precision of less than 1 \AA .

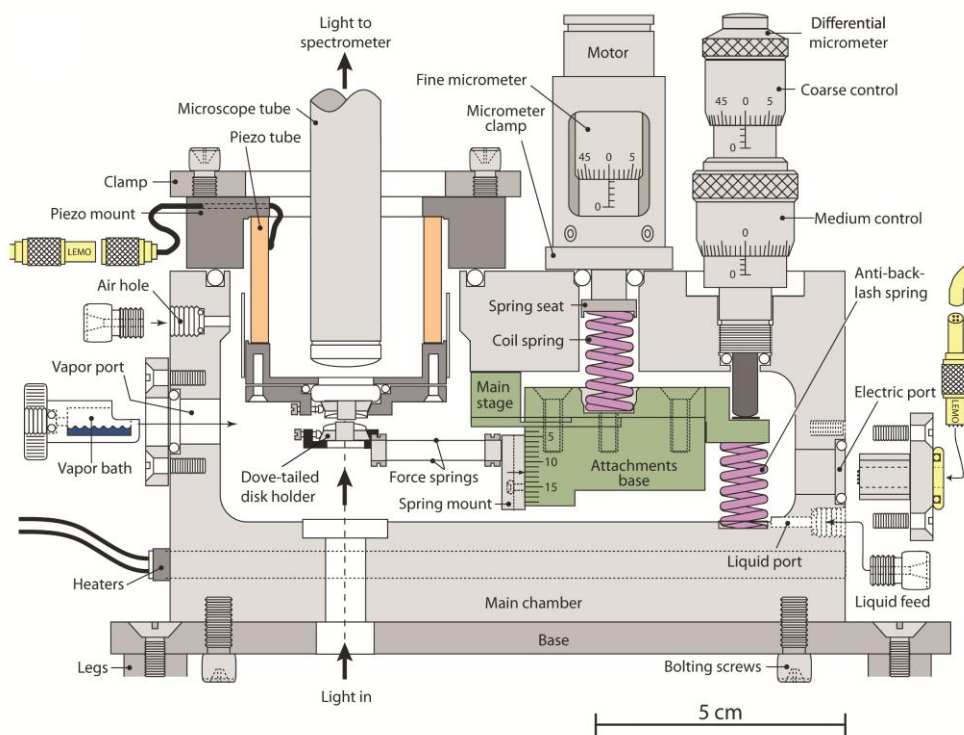


Figure 0.1 Schematic drawing of SFA 2000 [6]

Figure 0.2 shows a brief setup of a typical SFA experiment. Two back silvered molecular smooth mica surfaces are glued onto two cylindrical silica discs (of radius R). The two surfaces are placed in a crossed cylinder configuration which is locally equivalent to a sphere (of radius R) near a flat surface or to two spheres (of radius $2R$) close together when the separation distance $D \ll R$. The absolute surface separation distance can be monitored by using an optical technique called multiple beam interference (MBI), which is described in details in the next section. During experiments, white light passes normally through the two surfaces and the merging interference light beam is focused on the grating spectrometer which generates a series of Fringes of Equal Chromatic Order (FECO) [10, 11]. Typical FECO fringe pattern is shown in Figure 0.3.

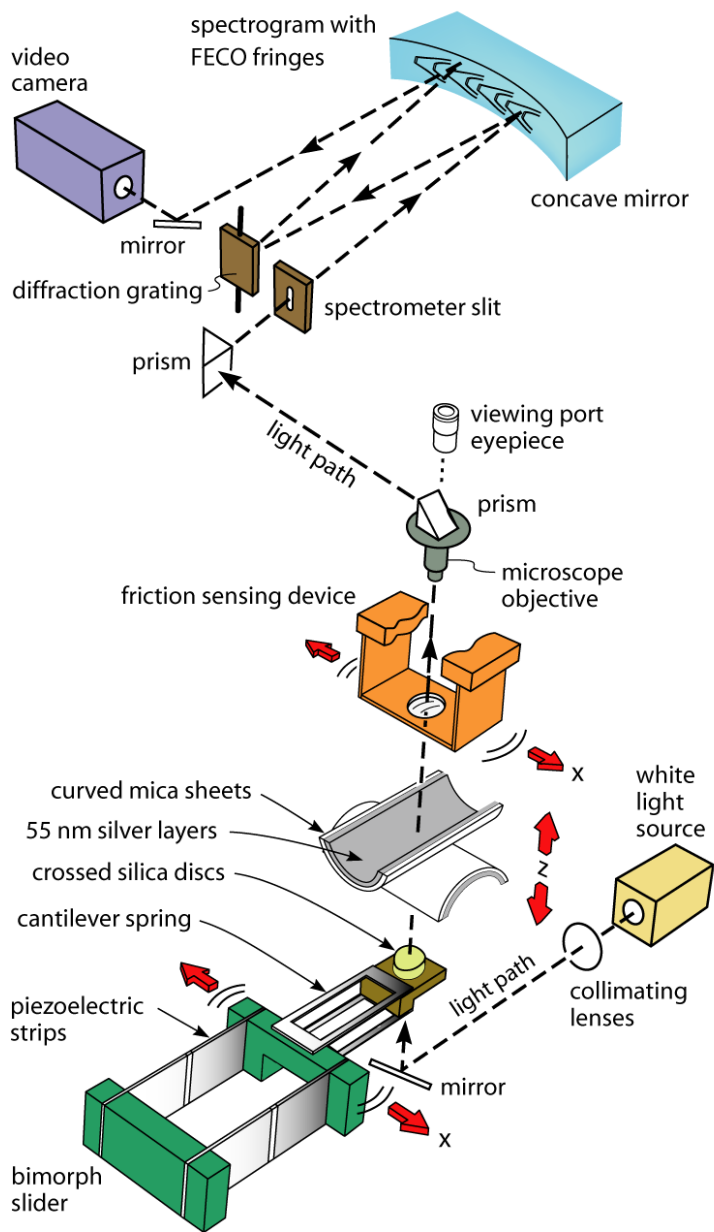


Figure 0.2 Schematic drawing of a typical SFA experimental setup

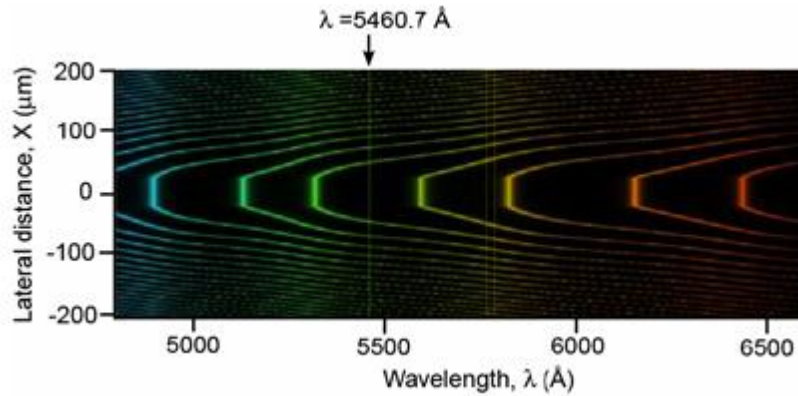


Figure 0.3 FECO fringes in a typical force measurement (two mica surfaces in adhesive contact)

1.4 Multiple beam interferometry (MBI)

MBI is an optical interference technique for measuring thickness and refractive index profiles of thin films, as described in details by S. Tolansky in 1948 and J. Israelachvili in 1973 [10]. MBI has been applied in SFA experiments for monitoring the film thickness, surface separation and deformations. In a typical SFA measurement, a pair of mica sheets is normally used as supporting substrates which are back coated with silver. When two surfaces come into contact and white light passes vertically through the two surfaces, the emerging interference light can be separated by a grating spectrometer into sharp fringes (FECO) consisting of discrete wavelengths λ_n^0 ($n = 1, 2, 3, \dots$), as shown in Figure 0.3. If the two mica sheets have the same thickness, the surface separation D and the fringe wavelength λ_n^D can be correlated by

$$\tan(2\pi\mu D / \lambda_n^D) = \frac{2\bar{\mu}\sin\left[\pi\left(1 - \lambda_n^0 / \lambda_n^D\right) / \left(1 - \lambda_n^0 / \lambda_{n-1}^0\right)\right]}{(1 + \bar{\mu}^2)\cos\left[\pi\left(1 - \lambda_n^0 / \lambda_n^D\right) / \left(1 - \lambda_n^0 / \lambda_{n-1}^0\right)\right] \pm (\bar{\mu}^2 - 1)}, \quad (2.1)$$

where ‘+’ refers to odd order fringes (n odd), and ‘-’ refers to even order fringes (n even). $\bar{\mu} = \mu_{mica} / \mu$, where μ_{mica} is the refractive index of mica at λ_n^D , and μ is the refractive index of the medium between the two mica surfaces at λ_n^D . For separation less than 30 nm, the Eq. (2.1) can be simplified to the following two approximate equations

$$D = \frac{nF_n(\lambda_n^D - \lambda_n^0)}{2\mu_{mica}} \quad \text{for n odd (positive sign in Eq.(2.1))} \quad (2.1a)$$

$$D = \frac{nF_n(\lambda_n^D - \lambda_n^0)\mu_{mica}}{2\mu^2} \quad \text{for n even (negative sign in Eq.(2.1))} \quad (2.1b)$$

where $F_n = \lambda_{n-1}^0 / (\lambda_{n-1}^0 - \lambda_n^0)$. By using the above equations, the distance D can be determined by measuring the shifts in wavelengths of an odd and adjacent even fringe. The accuracy is about 1 Å for measurement of D in the range of 0-200 nm.

The local radius of curvature of the surfaces is normally used to normalize the measured surface forces, which can be determined directly from the shape of the FECO fringes by measuring two distances D_1 and D_2 as well as the lateral distance X on any fringe as shown in Figure 0.4. If the spectrometer-microscope magnification factor is f , the radius $R_{||}$ is given by Eq. 2.2.

$$R_{\parallel} = \frac{(X / f)^2}{8(D_2 - D_1)} \quad (2.2)$$

R_{\perp} value is the radius measured perpendicular to R_{\parallel} using a DOVE prism, and the mean radius of curvature is given by $R = \sqrt{R_{\parallel}R_{\perp}}$ [12].

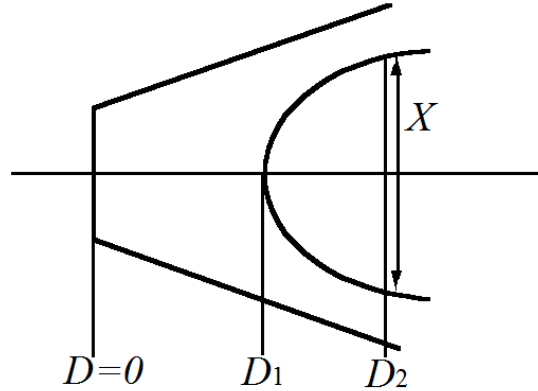


Figure 0.4 Schematic of FECO fringes to measure the radius of local curvature of two surfaces.

1.5 Mica sheets preparation

Due to its molecularly smooth nature, mica is one of the most commonly used substrates in surface forces measurements in SFA. The process of mica sheets preparation is described briefly below. Select a thick sheet of Ruby Muscovite mica, trim its edges with large strong scissors, and remove all excess edge flakes. Then a semi-thick sheet is cleaved from this sheet to expose two smooth clean and step-free surfaces. Check the freshly cleaved semi-thick sheet and chose one as a backing sheet. Hang the backing sheet vertically from a clip parallel to the air-flow direction in dust-free laminar flow hood. The others are chosen for further cleaving of much thinner and smaller sheets as substrate

surfaces for force experiment. The thin sheet should be peeled away very slowly, without tearing or sticking occurring. Then the Pt wire cutting method is used to cut the uniform part of the sheet from the whole thin sheet followed by placing the thin and uniform sheet onto the backing sheet.

Next, the exposed surfaces are silvered in a vacuum coating unit with a uniform thickness of ~50 nm. The schematic drawing for mica sheets preparation is shown in Figure 0.5. After silvering, the mica sheets are peeled off from the backing sheet and glued, silver back down, onto the cylindrically curved silica disks. After gluing, the two surfaces are mounted into the SFA chamber, and the reference distance is determined by the adhesive contact of two mica surfaces which can be used for the calculation of film thickness and gap distance changes in further experiments.

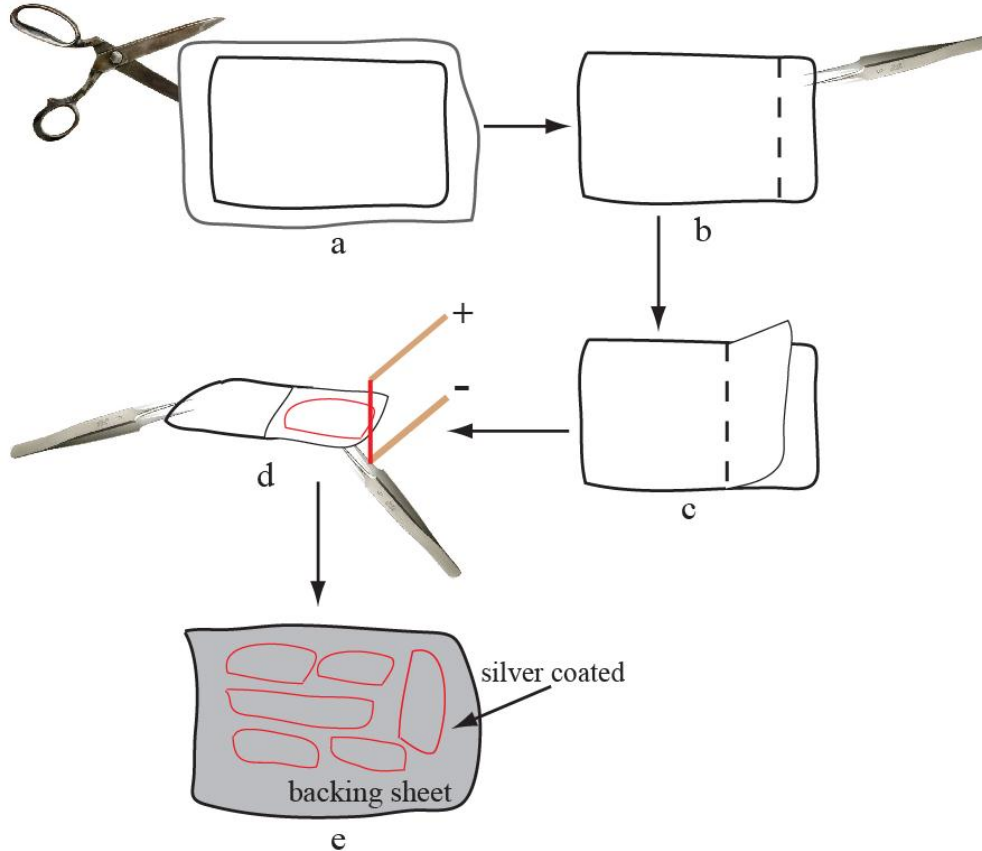


Figure 0.5 The schematic drawing of mica sheets preparation procedure: (a) trimming, (b) splitting, (c) peeling, (d) cutting and (e) silvering.

1.6 Normal force measurement

Normal forces between the surfaces are measured based on the Hooke's law, and the changed force $\Delta F = K_s \Delta x$, where K_s is the spring constant supporting the lower surface and $\Delta x = D_{applied} - D_{actual}$. The applied separation distance $D_{applied}$ is measured by the differential micrometer, motor-driven fine micrometer and piezoelectric crystal tube. The actual separation distance between two surfaces D_{actual} is determined by the MBI technique. The resolution of the

force measured using SFA is normally <10 nN and the accuracy of distance measurement is $<1 \text{ \AA}$ [11].

The normal force F is determined as a function of D , which is commonly normalized by the radius of curvature of the surfaces R . The adhesion forces are determined by multiplying the spring constant K_s with the distance that the two surfaces jump apart from the adhesive contact $F_{adhesion} = K_s \times D_{jump}$ as illustrated in Figure 0.6. The normalized force F/R of two curved surfaces can be correlated to the interaction energy per unit area between two flat surfaces by the Derjaguin approximation [11] (Eq. 2.3).

$$W_{flat}(D) = \frac{F(D)}{2\pi\sqrt{R_1R_2}} = \frac{F(D)}{2\pi R} \quad (2.3)$$

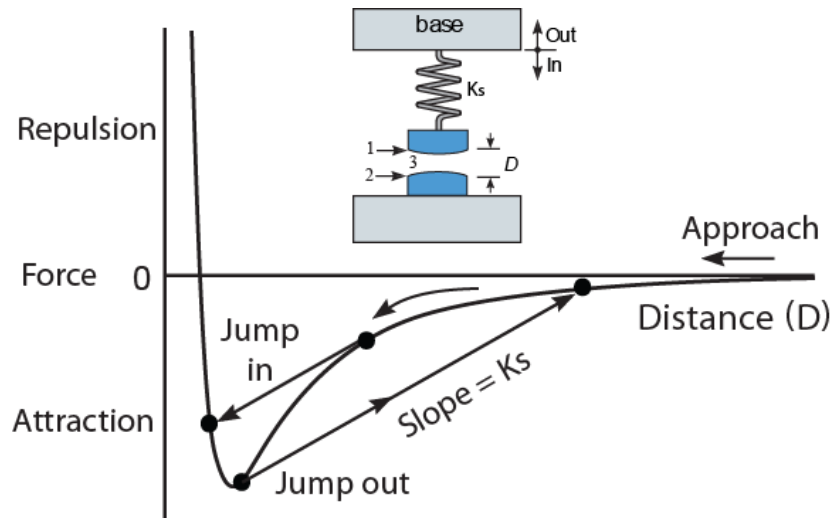


Figure 0.6 Schematic of the principle of normal force measurement.

1.7 Adhesion measurement using SFA (contact mechanics — JKR theory)

Surface energy γ is one of the most important parameters for characterizing surface properties. The surface deformation during contact and the adhesion between two purely elastic and smooth curved surfaces of the same materials can be described by the Johnson-Kendall-Roberts (JKR) theory given by Eq. 2.4 [13],

$$r^3 = \frac{R}{K} \left[F_{\perp} + 6\pi R\gamma + \sqrt{12\pi R\gamma F_{\perp} + (6\pi R\gamma)^2} \right] \quad (2.4)$$

where r is the contact radius, F_{\perp} is the applied load, and R is radius of local curvature.

The experimental procedure for determining the surface adhesion and surface energy is conducted as follows. Right after the two surfaces jump into contact, finite load is applied gradually to the lower surface against the upper surface till a maximum load is reached. Different waiting times can be chosen under the maximum load to investigate the time effect, and then tensile load is applied continuously till the two surfaces jump apart. During the loading-unloading process, the contact diameter ($2r$) is monitored as a function of the applied load (F_{\perp}) in real time through the FECO fringes. [14, 15], which forms the so-called “JKR plot”. The maximum tensile load where the two surfaces jump out is also recorded and referred as the adhesion force F_{ad} [16, 17].

The surface energy determined from the adhesion force (Eq. 2.5) usually coincides with the value obtained from the fitted loading curve for non-hysteretic systems (the adhesion energies difference of loading (advancing) and unloading (receding) paths, $\Delta\gamma = \gamma_R - \gamma_A$ is small).

$$\gamma = F_{ad} / 3\pi R \quad (2.5)$$

If a system is hysteretic ($\Delta\gamma > 0$), the unloading path cannot be fitted by the JKR model and an effective surface energy γ_{eff} is defined as $\gamma_{\text{R (non-JKR)}} = \gamma_{\text{eff}} = F_{ad} / 3\pi R$. It should be noted that normally the thermodynamic γ value can be still obtained from the fitting parameter of the loading curve using the JKR equation.

1.8 Other techniques

There are some other techniques used in this thesis research to investigate the surface/interfacial properties of solid surfaces or polymer thin films, including rheology measurement, atomic force microscopy (AFM), contact angle measurement, X-ray photoelectron spectroscopy (XPS), etc.

The viscosity measurement of a suspension is often used as a simple method to investigate the interactions between solids and a liquid medium. A rotational rheometer employing the cylinder geometry can be used to determine the viscosity of suspension. The working principle of rotational rheometer is briefly described as follows. A specific torque is applied to the suspension, and then the angular velocity can be obtained. Or an angular velocity is applied resulting in the determination of the torque. The applied torque can be varied in different experiments. Normally, a graph of apparent viscosity (η) versus shear rate ($\dot{\gamma}$) is plotted. The shear rate ($\dot{\gamma}$) and the shear stress (τ) can be determined by the angular velocity (ω) and the torque (T), respectively, and the viscosity can be obtained from the ratio between shear stress (τ) and shear rate ($\dot{\gamma}$). [18]

Atomic force microscopy (AFM) was invented by Binnig et al. in 1986. AFM has been widely used for over two decades for both force measurements and the imaging of various materials. The AFM consists of a cantilever with a sharp tip at its end that is used to scan the specimen surface. The cantilever is typically silicon or silicon nitride. When the tip is brought into proximity of a sample surface, forces between the tip and the sample lead to a deflection of the cantilever according to Hooke's law. The schematic of working principle of an AFM is shown in Figure 0.7. There are three modes of AFM: contact mode, non-contact mode, and tapping mode. Here the tapping mode is briefly described for obtaining the topography of surfaces. In this mode, the cantilever is externally oscillated at or close to its fundamental resonance frequency. An electronic feedback loop ensures that the oscillation amplitude remains constant, such that a constant tip-sample interaction is maintained during scanning. Forces that act between the sample and the tip will not only cause a change in the oscillation amplitude, but also change in the resonant frequency and phase of the cantilever. These changes in oscillation with respect to the external reference oscillation provide information about the sample's characteristics [19].

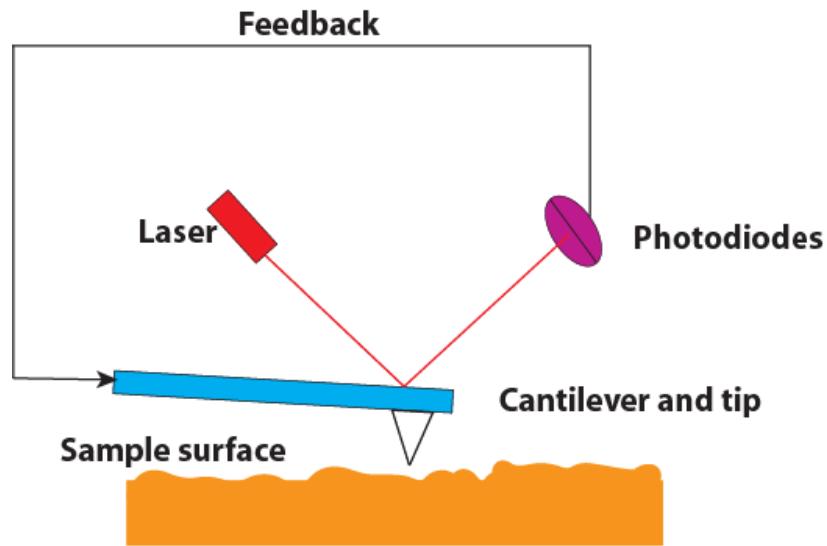


Figure 0.7 Schematic drawing of AFM working principle.

Contact angle θ is normally referred to the angle between a solid surface and a liquid as shown in Figure 0.8, which is related to the surface energy γ of solid substrate based on the Young equation (Eq. 2.6). If the liquid strongly affiliates the solid surface, the liquid drop will quickly and completely spread out on the solid. On the other hand, weak attraction between the liquid and solid normally results in a larger contact angle. Contact angle is commonly measured by the sessile drop method. By placing a liquid droplet on a solid surface, the equilibrium contact angle can be recorded and determined from the drop shape. More details are described in the experimental section in chapter 4.

$$\gamma_{SG} - \gamma_{SL} - \cos \theta \gamma_{LG} = 0 \quad (2.6)$$

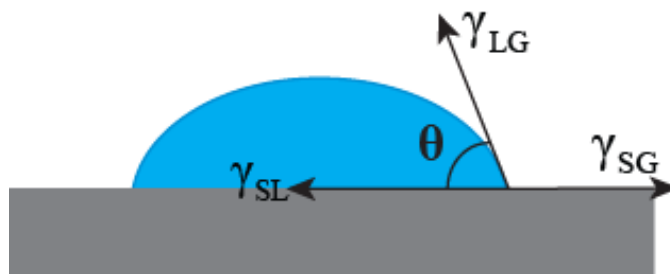


Figure 0.8 Illustration of contact angle of a liquid on a solid surface.

1.9 X-ray Photoelectron Spectroscopy (XPS)

X-ray Photoelectron Spectroscopy (XPS) is also known as electron spectroscopy for chemical analysis (ESCA). It is based on the photoelectric effect. Each atom in the surface has core electron with the characteristic binding energy that is considered equal to the ionization energy of that electron. When an X-ray beam directs to the sample surface, the energy of the X-ray photon is adsorbed completely by the core electron of an atom. If the photon energy, $h\nu$, is large enough, the core electron will then escape from the atom and emit out of the surface. The emitted electron with the kinetic energy of E_k is referred to as the photoelectron. The schematic of photoelectron emission process is shown in Figure 0.9. The binding energy of the core electron is given by the Einstein relationship:

$$h\nu = E_b + E_k + \phi \quad (2.7)$$

where $h\nu$ is the X-ray photon energy, E_k is the kinetic energy of photoelectron, which can be measured by the energy analyzer and ϕ is the work function induced

by the analyzer, about 4~5eV. Since the work function, ϕ , can be compensated artificially, it is eliminated, giving the binding energy as follows [20]:

$$E_b = h\nu - E_k \quad (2.8)$$

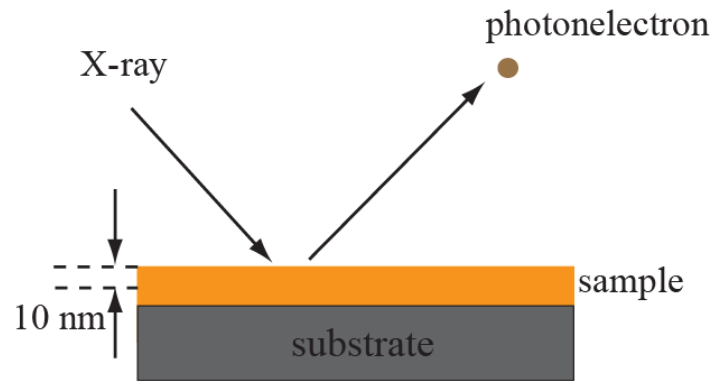


Figure 0.9 A brief schematic of photoelectron emission process.

References

- [1] D. Tabor, *Winterto.Rh, Proc R Soc Lon Ser-A*, 312 (1969) 435.
- [2] D. Tabor, *Chem Ind-London*, (1971) 969.
- [3] J.N. Israelachvili, G.E. Adams, *Nature*, 262 (1976) 773.
- [4] J.N. Israelachvili, *Faraday Discuss*, 65 (1978) 20.
- [5] J.N. Israelachvili, P.M. Mcguiggan, *J Mater Res*, 5 (1990) 2223.
- [6] J. Israelachvili, Y. Min, M. Akbulut, A. Alig, G. Carver, W. Greene, K. Kristiansen, E. Meyer, N. Pesika, K. Rosenberg, H. Zeng, *Rep Prog Phys*, 73 (2010).
- [7] J.N. Israelachvili, *Abstr Pap Am Chem S*, 198 (1989) 172.
- [8] J. Israelachvili, *P Natl Acad Sci USA*, 84 (1987) 4722.
- [9] P.M. Mcguiggan, J.N. Israelachvili, *J Mater Res*, 5 (1990) 2232.
- [10] Israelac.Jn, *J Colloid Interf Sci*, 44 (1973) 259.
- [11] J. Israelachvili, *Intermolecular and Surface Forces*, third ed., Academic Press, 2011.
- [12] Israelac.Jn, D. Tabor, *Proc R Soc Lon Ser-A*, 331 (1972) 19.
- [13] K.L. Johnson, K. Kendall, A.D. Roberts, *Proc R Soc Lon Ser-A*, 324 (1971) 301.
- [14] N. Maeda, N.H. Chen, M. Tirrell, J.N. Israelachvili, *Science*, 297 (2002) 379.

- [15] N.H. Chen, N. Maeda, M. Tirrell, J. Israelachvili, *Macromolecules*, 38 (2005) 3491.
- [16] H.B. Zeng, N. Maeda, N.H. Chen, M. Tirrell, J. Israelachvili, *Macromolecules*, 39 (2006) 2350.
- [17] H.B. Zeng, M. Tirrell, J. Israelachvili, *J Adhesion*, 82 (2006) 933.
- [18] M.M. Malik, M. Jeyakumar, M.S. Hamed, M.J. Walker, S. Shankar, *J Non-Newton Fluid*, 165 (2010) 733.
- [19] H. Kaczmarek, R. Czajka, M. Nowicki, D. Oldak, *Polimery-W*, 47 (2002) 775.
- [20] J.C. Vickerman, I. Gilmore, *Surface Analysis: The Principal Techniques*, 2nd ed., John Wiley and Sons, 2009.

CHAPTER 3 PROBING MOLECULAR AND SURFACE INTERACTIONS OF COMB-TYPE POLYMER POLYSTYRENE-GRAFT-POLYETHYLENE OXIDE (PS-G- PEO)¹

1.10 Introduction

Functionalities of polymer coatings play important roles in numerous engineering and biomedical applications, ranging from adhesion, lubrication, wettability control, drug delivery, stabilization/destabilization of colloids to antifouling treatments. Block copolymers are composed of blocks of different polymerized monomers. Amphiphilic diblock or tri-block copolymers, with both hydrophobic and hydrophilic units, have attracted much interest due to their interesting interfacial properties, i.e., interfacial aggregation behaviour, self-assembly in bulk solutions or on substrates, dewetting and surface interactions. An amphiphilic block polymer is able to adsorb or anchor one block onto a solid substrate while extend the other block into a favourable solution medium acting as a swollen brush layer with many important engineering applications. [1-14] For example, poly(ethylene oxide)/poly(propylene oxide)/poly(ethylene oxide) or PEO-PPO-PEO shows good potential in the development of polymeric additives for antifriction and/or antiwear, which has been studied in terms of its adsorption behaviour on different substrates, phase behaviours, morphology, and surface

¹ A version of this chapter has been submitted for publication. L. Zhang, H. Zeng, Q. Liu 2012. Journal of Physical and Chemistry, C (under review).

interactions. [2, 4, 6, 8-10] Diblock copolymer polystyrene/polyethylene oxide (PS-b-PEO), with various PEO contents and molecular weights, was extensively studied regarding to its properties at water-air interfaces using Langmuir Blodgett balance technique. [3-5, 7, 13] The micelle formation, self-assembly morphology and surface forces of PS-b-PEO in organic solvents have also been investigated. [11, 12]

During the past decade, comb-type copolymers have attracted much attention in polymer chemistry and physics, nanotechnology and bioengineering, which are special copolymers with many branches grafted to a polymer backbone. Comb-type amphiphilic copolymers have been considered as an alternative approach to amphiphilic block copolymers for hydrophobic drug solubilization and drug delivery. The comb-type copolymers can be fabricated with diverse architectures with multifunctionalities such as stimuli-responsive properties and site-specific targeting capabilities. Spencer and coworkers reported that Poly(L-lysine)-g-Poly(ethylene glycol) or PLL-g-PEG of different PLL/PEO ratios can adsorb on metal oxide surfaces, and the friction force and attachment mechanism of proteins on PLL-g-PEG layer were measured by using atomic force microscope (AFM) and pin-on-disk tribometry. [15-17] Brady et al. investigated the solvent-dependent friction force of poly(ethylenimine)-graft-poly(ethylene glycol) brushes using AFM. [18] Asatekin et al. studied the antifouling properties of membranes containing polyacrylonitrile-graft-poly(ethylene oxide). [19] Njikang et al. reported self-assembly behaviors of arborescent polystyrene-graft-poly(ethylene oxide). [20] In these early studies, polyethylene oxide (PEO) was

widely used which has been found to be promising in the development of functional brush copolymers/coatings with important bioengineering applications, e.g., antifouling. Although the applications of comb-shaped amphiphilic copolymers are rapidly increasing, understanding of their fundamental molecular interactions still remains limited.

In this work, the molecular interactions and surface properties of an amphiphilic comb-type copolymer with a polystyrene backbone and a polyethylene oxide side chains (PS-grafted-PEO or PS-g-PEO) were investigated using a surface forces apparatus (SFA) and an AFM, which provides new insights into the fundamental understanding of molecular and surface interaction mechanisms of comb-shaped copolymers and development of novel polymers and coatings with antifriction or antifouling properties.

1.11 Materials and Experimental Methods

1.11.1 Materials and samples preparation

Polystyrene-g-poly(ethylene oxide) (PS-g-PEO) comb-type copolymer (number average molecular weight $M_n = 24500$ g/mol, M_n of the polymer backbone is ~ 6000 g/mol, M_n of each PEO branch is ~ 4500 g/mol, average number of monomers on each PEO branch chain is ~ 102.3 , polydispersity $M_w/M_n = 1.6$) was purchased from Polymer Source Ltd. and used as received. The chemical structure of PS-g-PEO is shown in Figure 0.1. High-performance liquid chromatography (HPLC)-grade toluene purchased from Fisher Scientific was used as received. Ruby mica sheets were purchased from S & J Trading Inc. (Glen Oaks, NY). High-purity anhydrous sodium chloride (Sigma-Aldrich, 99.999

+ %) was used as received. Milli-Q water with a resistance of $\geq 18.2 \text{ M}\Omega\cdot\text{cm}$ was used for preparing the aqueous solutions needed.

PS-g-PEO film was prepared by spin coating method. Briefly, PS-g-PEO was first dissolved in toluene to prepare a 0.5 wt% solution. Freshly cleaved mica sheets were used as supporting substrates for preparation of polymer thin films by spin coating ($\sim 1000 \text{ rpm}$ for about 40s). The thin film samples were dried under reduced pressure ($\sim 50 \text{ mmHg}$) overnight ($>12 \text{ h}$) to remove the solvent, and then used for contact angle, topographic imaging and surface forces measurements. The thickness of polymer films used in this study was controlled about 15-30 nm which did not show significant impact for the results obtained. The polymer film thickness was measured in situ using an optical interferometry employing fringes of equal chromatic order (FECO) in the SFA. The polymer film thickness was also confirmed by spin coating a film on silicon wafer cleaned with ethanol and UV/Ozone cleaner and then determined using a Sopra GESp-5 spectroscopic ellipsometer (France).

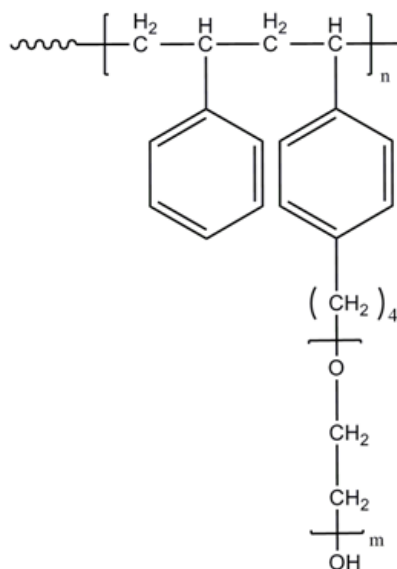


Figure 0.1 Chemical structure of comb-type polymer PS-g-PEO used in this study.

1.11.2 Surface force measurement in aqueous solution using SFA

Surface forces apparatus (SFA) has been widely applied to measure physical forces between surfaces in many biological and non-biological systems. [21-28] An SFA was used in this study to measure the interaction forces of PS-g-PEO film in NaCl solution. The detailed setup for SFA experiments has been reported elsewhere. [29-33] Briefly, two back silvered thin mica sheets (1–5 μm) were glued onto cylindrical silica disks (radius $R = 2$ cm). The PS-g-PEO film was spin coated on the mica following the aforementioned method. The two surfaces were then mounted in the SFA chamber in a crossed-cylinder configuration which was locally equivalent to a sphere of radius R interacting with a flat surface or two spheres of radius $2R$ when the surface separation D was much smaller than R ($D \ll R$). SFA measures the interaction forces F between the curved surfaces as a function of absolute surface separation distance D with force and distance resolutions down to <10 nN and 0.1 nm, respectively. During SFA experiments,

the absolute surface separation can be monitored in real-time and in situ by using multiple beam interferometry employing fringes of equal chromatic order (FECO).

[34]

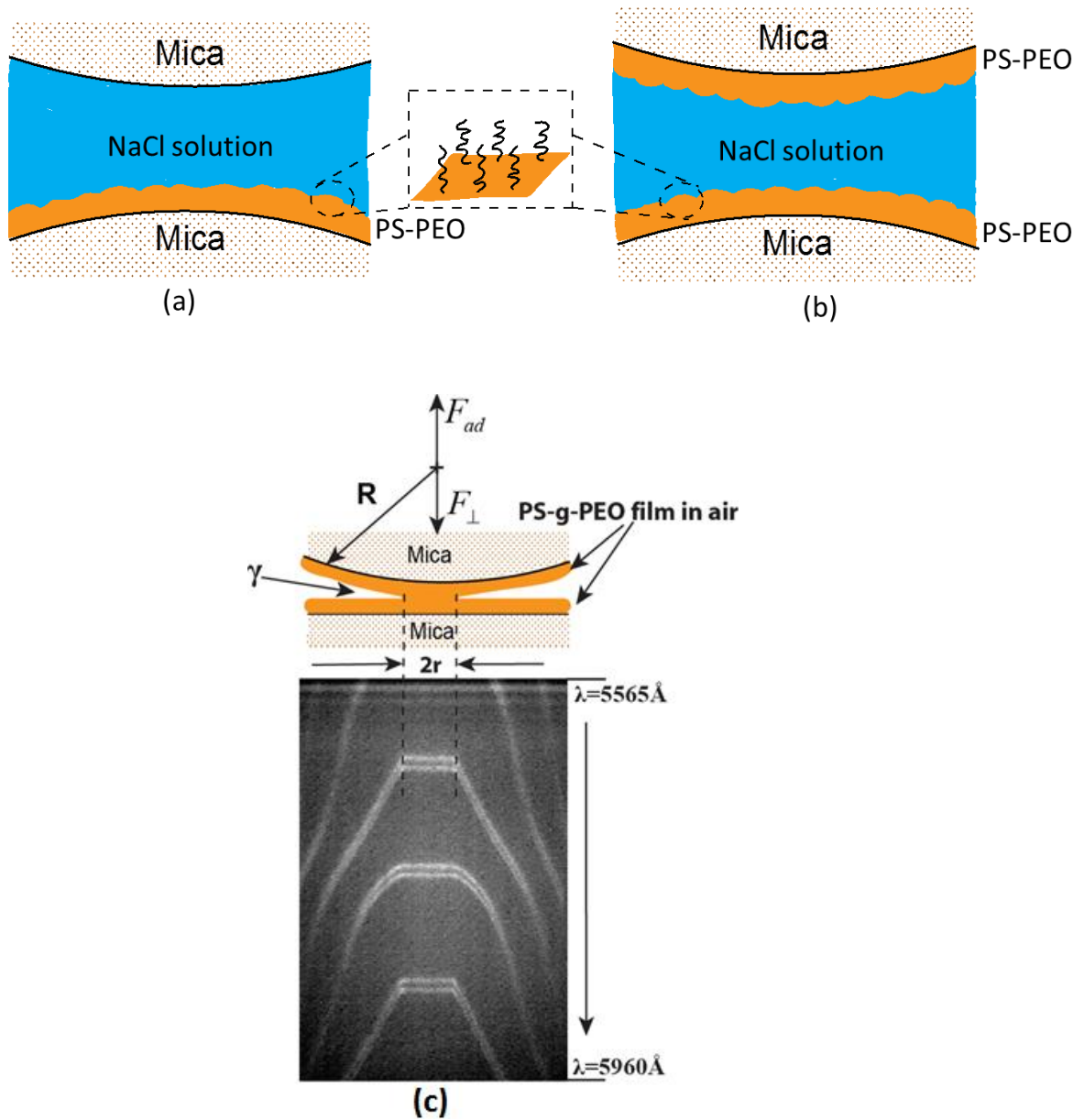


Figure 0.2 Experimental configurations of surface forces measurement: (a) PS-g-PEO film coated on mica surface versus a bare mica surface in NaCl solution (asymmetric case), (b) two PS-g-PEO films coated on two mica surfaces in NaCl

solution (symmetric case), (c) schematic of two polymer surfaces in adhesive contact in air and typical FECO fringes.

In this study, the interaction forces of PS-g-PEO were measured in 1 mM and 100 mM NaCl solution by SFA in two different configurations as shown in Figure 0.2: (a) a PS-g-PEO polymer film versus a bare mica surface (asymmetric), and (b) two opposing PS-g-PEO films (symmetric). The thickness of dry polymer film was measured by using the mica-mica adhesive contact as a reference. During force measurement, the reference distance ($D = 0$) was determined at the adhesive contact between a bare mica surface and a polymer surface (asymmetric case) or between the two polymer surfaces (symmetric case) in air. The surface force measurements were repeated for at least three independent pairs of samples with three different interaction positions for each pair of samples under a fixed experimental condition.

1.11.3 Adhesion measurement (contact mechanics) in air using SFA

The adhesion of PS-g-PEO films in air and the surface energy of comb-type polymer were determined by contact mechanics test using an SFA. The contact mechanics tests on the polymer surfaces were done for dry (and smooth) polymer films (in order to obtain the surface energy, it should be noted that the recent report by Benz et al. showed roughness plays a critical role in the contact mechanics of polymer surfaces [35]). The experimental setup of contact mechanics measurement in SFA has been described in details previously. [36, 37] Briefly, two PS-g-PEO films coated on mica were brought into adhesive contact in air in the SFA, and then finite compressive load was applied. The contact area

(or contact diameter $2r$) was monitored through FECO fringes (see Figure 0.2c) with increasing load F_{\perp} in real time till a maximum load ($F_{\perp, \max} \sim 35.3$ mN in this study) was reached. Then unloading process was initiated by gradually reducing the compressive load till the two surfaces were separated (jumped apart) under a critical tensile load which was referred as the adhesion force F_{ad} . The contact mechanics (contact diameter versus applied load) and adhesion were then analyzed using the Johnson-Kendall-Roberts (JKR) theory, and adhesion energy of the polymer surface was obtained. [38, 39]

1.11.4 Contact angle measurement

The contact angle of water on PS-g-PEO surface was measured by a sessile drop method using a Krüss drop shape analysis system (DSA 10-MK2, Germany). A Milli-Q water sessile drop was placed on the sample surface, and the interaction process between water drop and polymer surface was recorded by a video camera. The video was then converted to images and the contact angle was determined by fitting the shape of the sessile drop on the polymer surface. The contact angles of three different probe liquids (water, ethylene glycol and glycerol) were also measured. The Good-Van Oss model [40, 41] was applied to determine the surface energy of the PS-g-PEO film.

1.11.5 AFM imaging

Surface morphology and roughness of PS-g-PEO films with and without water treatment were characterized using an AFM in tapping mode (Agilent technologies 5500, Agilent, Santa Barbara, CA, USA). The impact of water on

surface morphology of PS-g-PEO was investigated by immersing the polymer film in Milli-Q water for 30 min. The polymer film (after the exposure to water) was dried under reduced pressure (~50 mmHg) for ~30 min before AFM imaging. At least three samples (1 cm ×1 cm) were imaged at different (>5) positions of the same surface under each condition, and the typical images were presented.

1.11.6 X-ray photoelectron spectroscopy (XPS)

XPS was employed to determine the top surface chemical composition of PS-g-PEO films. 1 cm × 1 cm polymer film samples were prepared for the XPS measurements which were performed at Alberta Center for Surface and Engineering Science (ACES) using Kratos Axis Ultra Spectrometer employing a monochromated Al-K α X-ray source ($h\nu = 1486.71$ eV). The spectrometer was calibrated with the binding energy (84.0 eV) of Au 4f_{7/2} with reference to Fermi level. The pressure of analysis chamber during experiments was controlled below 5×10^{-10} Torr. A hemispherical electron-energy analyser working at the pass energy of 20 eV was used to collect core-level spectra while survey spectrum within a range of binding energies from 0 to 1100 eV was collected at analyser pass energy of 160 eV. Charge effects were corrected by using C 1s peak at 284.8 eV. A Shirley background was applied to subtract the inelastic background of core-level peaks. Non-linear optimization was used to determine the peak model parameters such as peak positions, widths and peak intensities by using the Marquardt Algorithm (Casa XPS).

1.12 Results and Discussion

1.12.1 Characterization of PS-g-PEO polymer film

AFM images of spin-coated PS-g-PEO film and the polymer film after treated with water are shown in Figure 0.3 (a) and (b). The spin-coated PS-g-PEO film has a root-mean-square (rms) roughness of ~ 1.2 nm. After the polymer films were exposed to water for 30 min and fully dried, the surface became rougher and the rms roughness increased to ~ 7.0 nm. Interesting polymer surface patterns were also observed after water treatment (in Figure 0.3b). Similar surface patterns and polymer aggregation were previously reported for amphiphilic block polymers at air/water interface and in bulk solutions, which are mainly due to the intermolecular and intramolecular interactions of amphiphilic polymer segments and solvents and significantly depend on the polymer molecular structure, molecular weight and solution conditions. [42-45] A complete investigation on the evolution of surface pattern and molecular conformation of comb-type PS-g-PEO polymer in water and at water/air interface and the impact of molecular weight and structure will be reported in a separate study. Contact angle measurements were used to evaluate the hydrophilicity of the PS-g-PEO surfaces. The contact angle of water on the PS-g-PEO film and its evolution with time are shown in Figure 0.4. The spin-coated PS-g-PEO film showed an initial water contact $\sim 66^\circ$, which decreased sharply by over 10° in less than one second and then gradually reached $\sim 37^\circ$ in about 60 s. The contact angle did not change with further increasing time. The decrease of the water contact angle indicates the PS-g-PEO surface turned more hydrophilic after it was exposed to water because of

the strong interactions between hydrophilic PEO side chains and water molecules governed by hydrogen bonding and van der Waals forces. It is mostly likely that after contacting with water, the PEO chains became fully hydrated and tended to extend out from the solid surface into the water phase, and such conformation rearrangement also contributed to surface roughness change as shown in the AFM images (Figure 0.3).

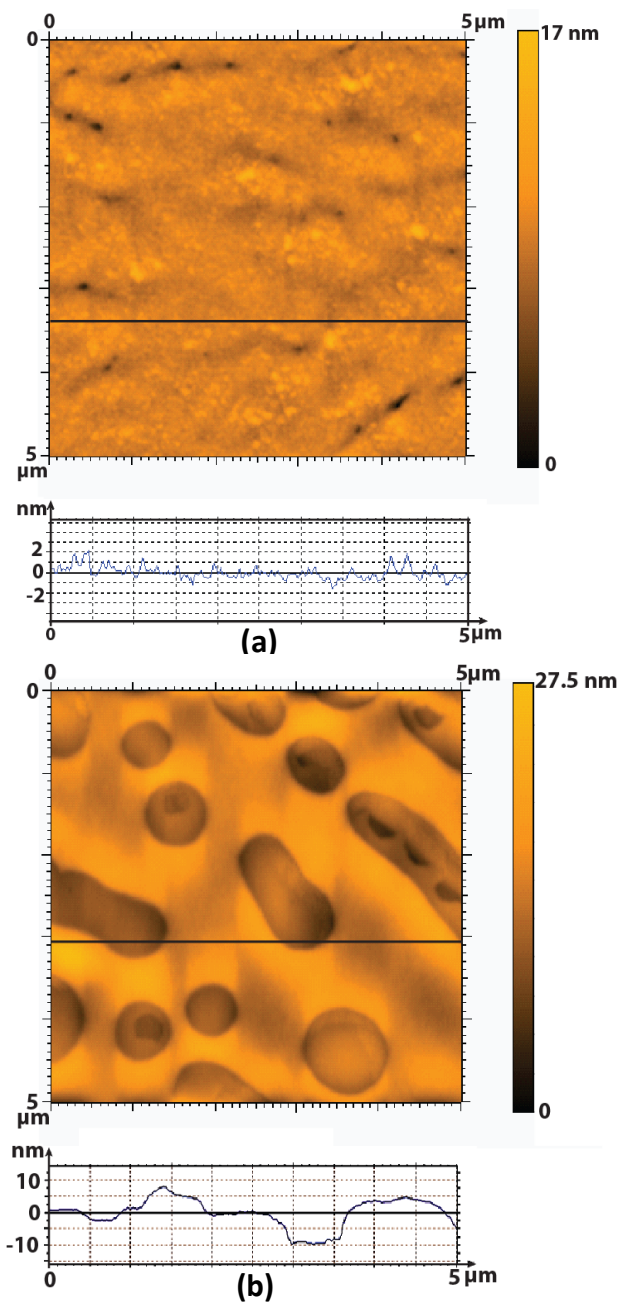


Figure 0.3 The AFM images of PS-g-PEO film (a) before treatment, (b) after water treatment.

XPS tests were performed on both spin-coated PS-g-PEO film and the film treated by water (results shown in Supplementary Information). The surface after water treatment was kept in vacuum and the XPS test was conducted after ~25

hours. Two main peaks were detected in the XPS spectrum, corresponding to the C1s and the O1s signals. Although the C/O ratios were slightly different for untreated and treated samples (discussed below), the measured C1s and O1s core level spectra were identical as shown in Figure S0.1 (for untreated PS-g-PEO surface). As shown in Figure S0.1a, the C1s peak can be fitted with two subpeaks: peak a centered at 285.7 eV which is attributed to the carbons in the styrene unit, and peak b centered at 287.4 eV corresponding to C-O carbons on the PEO side chains. Figure S0.1b shows the O1s spectra from C-O oxygen with energy peak centered at 533.5 eV. The XPS results indicate that both PS and PEO are present within the top surface of polymer film being probed. The XPS analysis also shows that the amount of O increased from 15.1 ± 0.2 at% for original spin-coated polymer surface to 16.3 ± 0.2 at% after the surface was treated by water. Such a small increase (~ 1.2 at%) of O content was mainly due to conformation rearrangement of PS-g-PEO molecules in the interfacial layer after the polymer surface was exposed to water and the PEO branches extended into the solution phase. It should be noted that O content determined by XPS on polymer surface after water treatment is still much lower than that in PEO chains (~ 33 at%), which may be caused by two factors: (1) XPS can detect the elements only on the top polymer layer of several nm (normally up to ~ 10 nm) and the element content determined was an average of the whole interfacial layer (not only the upmost surface), and (2) the XPS tests were conducted on dry polymer samples after kept in vacuum for ~ 25 hrs during which period some of hydrophobic polystyrene units/segments might rearrange and migrate back to surface layer.

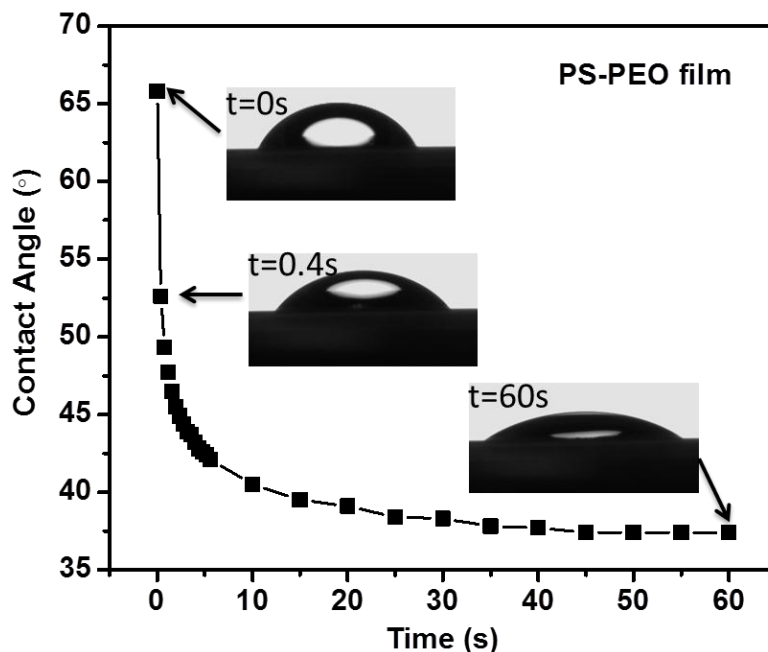


Figure 0.4 Contact angle of water on spin-coated PS-g-PEO film.

1.12.2 Interaction forces between PS-g-PEO films in NaCl solution

Surface force measurements were conducted to elucidate how PS-g-PEO polymer surface interacts with each other or with an opposing substrate in aqueous solution. Figure 0.5a and b shows the normalized force-distance profiles between two PS-g-PEO films (symmetric configuration) and between a PS-g-PEO film and mica surface (asymmetric configuration) measured in 1 mM and 100 mM NaCl solution, respectively. The asymmetric experiment (polymer vs. mica) was intended to investigate the surface interaction between a thin film of comb-type polymer (PS-g-PEO) and a model molecularly smooth clay surface, while the symmetric experiment (polymer vs. polymer) was designed to investigate the

intermolecular interactions of the PS-g-PEO, which could provide some insights into the molecular and surface interaction mechanisms of the comb-type polymer.

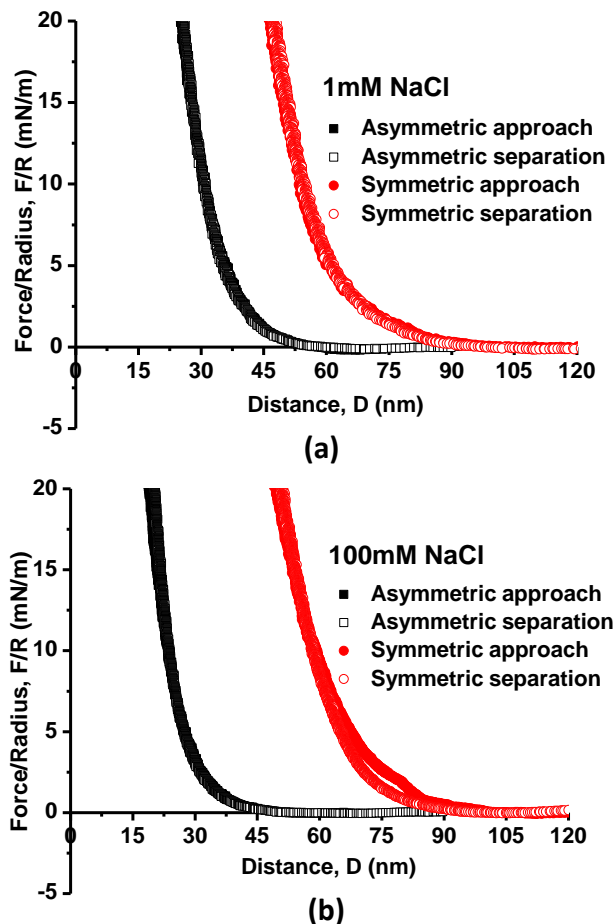


Figure 0.5 Force-distance profiles between a PS-g-PEO polymer film and a bare mica surface (asymmetric configuration) and between two PS-g-PEO polymer films (symmetric configuration) in aqueous solution of (a) 1 mM NaCl (b) 100 mM NaCl.

Several interesting features can be observed from the force-distance profiles for both symmetric and asymmetric configurations. (1) Only pure repulsive forces were measured during both approach and separation. (2) No adhesion hysteresis was observed during the force measurement, e.g., the force-distance profiles

obtained during approach and separation almost overlap, which is mainly attributed to the large excluded volume of the hydrated PEO chains and the steric repulsive forces between the swollen PEO chains, thus hindering the interdigitation. [46-48] Such non-hysteretic behaviour of PEO chains has been previously reported for several PEO associated polymer/biopolymer systems, and PEO chains/coatings are also well known for their anti-fouling properties to some other polymers/biopolymers. [46, 49] However, it should be noted that shearing, long contact time and increased temperature could induce the hysteretic behaviour of PEO chains in certain systems. [46, 47, 49, 50] (3) The force-distance profiles measured in 1 mM and 100 mM NaCl are very similar, which indicates ionic strength of solution has no significant impact on the interaction forces of polymer surfaces. The small difference on the force-distance profiles during approach and separation at high ionic strength for the symmetric case was not considered to be significant. The force-distance profiles almost overlap at high load, and the small difference at low load might be due to the conformational difference and change of the swollen PEO chains under compression associated with approach and separation. More importantly, no adhesion nor significant adhesion hysteresis were observed, which indicates that the steric interaction between the swollen PEO chains dominated the surface interaction, and interdigitation or interpenetration of the PEO chains on the two opposing surfaces was very limited. (4) The thickness of confined polymer layer between the two mica surfaces increased after the polymer surfaces were exposed to NaCl aqueous solution. In other words, the polymer films appeared “thicker” in the aqueous

solution than in the dry state. The distance $D=0$ in Figure 0.5 was referred as the adhesive contact between bare mica and dry polymer surface or between two dry polymer surfaces in air. D shifted to ~ 20 nm and ~ 45 nm for asymmetric and symmetric configurations, respectively, which is higher than the height change from AFM imaging. The AFM imaging of polymer surface was taken in air where the film (after water treatment) under dry condition, while the surface forces were measured in aqueous solution. Thus, the thickness change of the swelling polymer film in aqueous solution would be expected to be larger than that in fully dried state. The shift of the thickness of confined polymer was most likely due to the swelling of hydrophilic PEO side chains and molecular conformation rearrangement of the comb-type polymers leading to surface morphology change, which is consistent with the observations from contact angle measurement and AFM imaging. As shown in the contact angle measurements, it is suggested that hydrophilic PEO side chains may extend out from the polymer film into water and act as swollen brushes which makes the surface more hydrophilic. The fully extended length H_{\max} of the PEO side chain can be estimated based on the molecular weight of PEO or number of repeat PEO units by Equation 1 as $H_{\max} \approx 25.7$ nm, which gives fully extended polymer chain length with a planar freely-jointed zigzag conformation, where $m \approx 102.3$ is the average number of repeat PEO units in a side chain, $l \approx 1.54 \text{ \AA}$ is the bond length and $\theta \approx 109.5^\circ$ is the bond angle. [51] Figure 0.3 shows that the polymer surface becomes rougher after exposed to water, and the peak-peak roughness (normal distance between the lowest and highest points) is ~ 18 nm as shown in the extraction profile in Figure

0.3b. Thus, the sum of the peak-peak surface roughness and fully extended PEO chain length gives ~44 nm (~18 nm plus ~26 nm) for a single polymer film (asymmetric case), and ~90 nm for two polymer films (symmetric case). It should be also noted that the AFM imaging in Figure 0.3b was done in air after the film was dried, and the polymer film would be swollen in water leading to a longer range of interaction. The above estimated values were close to the range of repulsive forces measured in Figure 0.5 (e.g., ~50 nm and ~100 nm for asymmetric and symmetric configurations, respectively).

$$H_{\max} \approx 2ml \sin\left(\frac{\theta}{2}\right) \quad (1)$$

For the asymmetric case, mica is still charged under the solution conditions investigated. In 1 mM and 100 mM NaCl solution, the electric double layer Debye length was $\kappa^{-1} = 0.304/\sqrt{[\text{NaCl}]} = 9.6$ and 0.96 nm respectively ($[\text{NaCl}]$ in M), which are much less than the fully extended length of the neutral PEO side chain ~26.0 nm. Therefore, the electric double layer forces and the impact of the charged mica substrates are negligible, and the steric effect dominates the interactions between PS-g-PEO and mica.

In order to understand the nature of steric hindrance resulted from the PEO brushes, the measured force-distance profiles were fitted using the Alexander–de Gennes (AdG) scaling theory, which describes the steric forces between surfaces covered with end-tethered, monodisperse and neutral polymer brushes. [29, 52, 53] When two polymer brush layers approach each other and overlap, the increased local density of polymer segments lead to an increase in osmotic

pressure and repulsive interaction energy. The AdG theory predicts that the repulsive pressure between two planar brush layers can be described by Equation 2, where s is the mean distance between anchoring (or grafting) sites on the surface, L is the brush layer thickness per surface, k is Boltzmann constant and T is temperature. [52]

$$P(D) \approx \frac{kT}{s^3} \left[\left(\frac{2L}{D} \right)^{9/4} - \left(\frac{D}{2L} \right)^{3/4} \right] \text{ for } D < 2L, \quad (2)$$

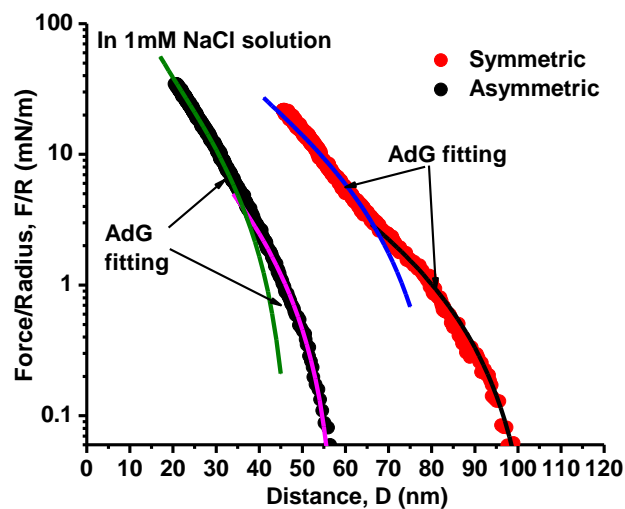
In SFA measurements, the geometry of crossed cylinders (of radius R) is commonly used, and the surface forces between two brush layers (symmetric configuration) can be given by Equation 3 by using the Derjaguin approximation. [29] For a brush layer interacting with a solid substrate (asymmetric configuration), the surface forces can be predicted by Equation 4.

$$\frac{F(D)}{R} = 2\pi \int P(D) dD = \frac{16\pi kTL}{35s^3} \left[7 \left(\frac{2L}{D} \right)^{5/4} + 5 \left(\frac{D}{2L} \right)^{7/4} - 12 \right] \quad (3)$$

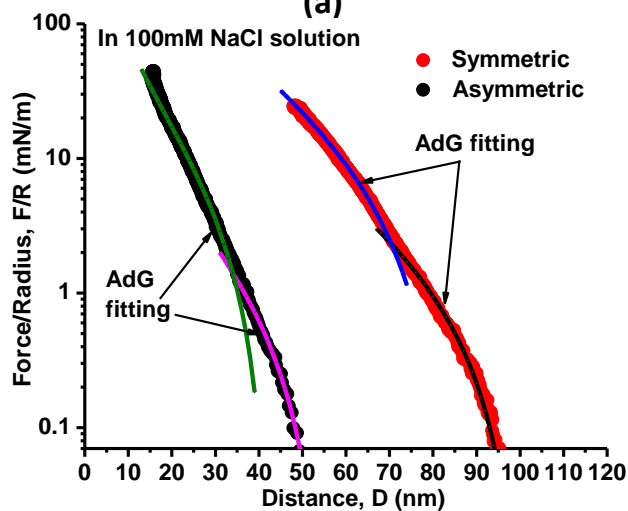
$$\frac{F(D)}{R} = \frac{8\pi kTL}{35s^3} \left[7 \left(\frac{L}{D} \right)^{5/4} + 5 \left(\frac{D}{L} \right)^{7/4} - 12 \right] \quad (4)$$

Figure 0.6a and b show the fit of measured repulsive forces of PS-g-PEO films with the AdG theory (solid curves) in both symmetric and asymmetric configurations in 1 mM and 100 mM NaCl solutions, respectively. It was found that the AdG theory (Equations 3 and 4) can well describe the measured steric forces at long separation distance under low compression forces, which confirms that the PEO branches of the comb-type PS-g-PEO extend into water and act as swollen brushes and further indicates that the measured repulsive forces have a steric nature. However the AdG fitting using one set of parameter (L , s) clearly

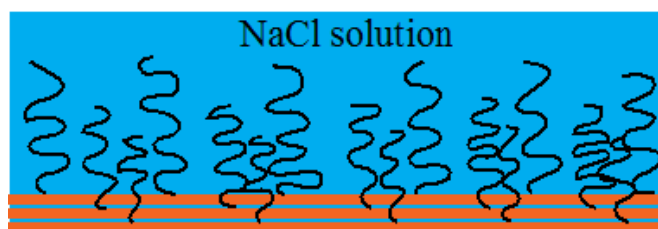
deviates from the experimental data at high load regime, as shown in the Figure S0.2 in Supplementary Information. Such deviation could be resulted from two aspects: (i) the PEO side chains from both polymer-water interface and sublayers can extend into water and the swollen PEO chains were not monodisperse brushes, as illustrated in Figure 0.6c (it is noted that Figure 0.6c was simply proposed to illustrate the possibility of swelling of PEO side chains in water from upmost polymer-water interface and sublayers in the polymer film, and the actual conformations could be more complex.); (ii) the conformation of PEO chains and local segment density increased with applied load while the surface morphology might also change with increasing load. Thus two independent sets of fitting parameters were used to better fit the force-distance curves at both low and high compression regimes (in Figure 0.6). The values of fitted parameters s and L are summarized in Table 1. It should be noted that the parameter s in the Alexander–de Gennes (AdG) theory stands for the mean distance between grafting sites of polymer brushes (while not the grafting density). Therefore the s value would decrease under higher compression. As shown in Table 0.1, the s value at short distance in the high load regime is close to half of that at long distance in the low load regime (for example, $s=6.6$ nm and 3.9 nm in the low and high load regimes, respectively, for asymmetric configuration in 1 mM NaCl shown in Figure 0.6a), indicating a much denser brush layer under higher load conditions.



(a)



(b)



(c)

Figure 0.6 Experimentally measured force-distance profiles (dot plots) for PS-g-PEO vs mica (asymmetric configuration) and two PS-g-PEO surfaces (symmetric configuration) and theoretically fitted curves using the Alexander-de Gennes (AdG) theory in (a) 1 mM NaCl and (b) 100 mM NaCl solution. (c) Illustration of

swollen PEO branches in water from polymer-water interface and sublayers in the polymer film.

Table 0.1 Fitting parameters using the Alexander-de Gennes Theory for experimentally measured force-distance profiles at both high and low compression regimes in Figure 0.6.

		1 mM NaCl		100 mM NaCl	
		High	Low	High	Low
		loading	loading	loading	loading
Asymmetric	L (nm)	48	59	42.1	54.9
	s (nm)	3.3	5.1	3.7	6.9
Symmetric	L (nm)	42	52.6	41.5	50
	s (nm)	3.9	6.6	3.3	5.8

1.13 Surface energy of PS-g-PEO film

1.13.1 Contact mechanics test

In order to fully understand the surface interactions and properties of PS-g-PEO, the adhesion and surface energy of PS-g-PEO surfaces in air was determined through contact mechanics test by following the widely used Johnson-Kendall-Roberts (JKR) adhesion test. [54-56] The contact radius between two PS-

g-PEO surfaces monitored through the FECO fringes in real time were plotted as a function of the applied load for both loading and unloading processes, as shown in Figure 0.7. It is interesting to note that the loading and unloading plots do not overlap and follow the same path and adhesion hysteresis is observed. The contact radius during the unloading process is larger than that during loading under the same compressive load, and a finite tensile load is needed to separate the two surfaces, commonly referred as the adhesion force, $F_{ad} \approx -9$ mN. The JKR model is also applied to better understand the contact and adhesion behavior of PS-g-PEO surfaces observed. [54, 57] According to the JKR model, when two purely elastic curved surfaces are pressed against each other by an external load F_{\perp} , the relation between contact radius r and load F_{\perp} can be described by Equation 5, where W is the adhesion energy (for two surfaces of the same material $W=2\gamma$, and γ is the surface energy), K is the equivalent modulus which is related to the Young's moduli E_1 and E_2 , and Poisson's ratios ν_1 and ν_2 by Equation 6, and R is the radius of local curvature given by Equation 7. [54]

$$\begin{aligned} r^3 &= \frac{R}{K} \left(F_{\perp} + 3\pi RW + \sqrt{6\pi R F_{\perp} W + (3\pi RW)^2} \right) \\ &= \frac{R}{K} \left(\sqrt{F_{\perp} + 3\pi RW/2} + \sqrt{3\pi RW/2} \right)^2 \end{aligned} \quad (5)$$

$$\frac{1}{K} = \frac{3}{4} \left(\frac{1-\nu_1^2}{E_1} + \frac{1-\nu_2^2}{E_2} \right) \quad (6)$$

$$\frac{1}{R} = \frac{1}{R_1} + \frac{1}{R_2} \quad (7)$$

$$F_{ad} = 3\pi RW_{ad} / 2 \quad (8)$$

In JKR tests, the adhesion hysteresis can be defined as $\Delta\gamma = (\gamma_R - \gamma_A) \geq 0$, where γ_A is the advancing surface energy on loading, and γ_R is the receding energy on unloading. $\Delta\gamma$ is a measure of the energy dissipated during a complete loading-unloading cycle. [54, 58, 59] For non-hysteretic systems, the loading and unloading paths are the same where $\Delta\gamma=0$ and $\gamma_A = \gamma_R = \gamma$, and the JKR Equation shows that the surfaces will detach or jump apart at a critical tensile load which gives the adhesion or ‘pull-off’ force F_{ad} as shown in Equation 8. For two surfaces of the same materials, the surface energy of the materials can be determined by $\gamma = \gamma_A = \gamma_R = W_{ad}/2 = F_{ad}/3\pi R$. However, in hysteretic systems such as polymers of low molecular weight, the loading (advancing) and unloading (receding) paths are not the same, as the case for PS-g-PEO in this study. As shown in Figure 0.7, the loading path can be fitted reasonably well with the JKR model (Equation 5) because γ_A is usually insensitive to different surface treatments of polymer surfaces and the surface energy obtained from the JKR fitting is often close to the thermodynamic value γ , [36] while the unloading path cannot be fitted due to the adhesion hysteresis. The fitted value from the loading path was considered to be close to the thermodynamic surface energy of the PS-g-PEO film, [36] which was compared with the value obtained from the contact angle measurement. While the receding energy on unloading was also shown and compared with the advancing energy, which was to show the adhesion hysteresis. The JKR fitting for the loading path leads to $\gamma = \gamma_A = 37.0 \text{ mJ/m}^2$ which can be considered as the thermodynamic surface energy of the PS-g-PEO film. The

receding energy on unloading (also referred as effective surface energy) can be given by the adhesion force measured as $\gamma_R = F_{ad}/3\pi R \approx 47.7 \text{ mJ/m}^2$, and the adhesion hysteresis is $\Delta\gamma \approx 10.7 \text{ mJ/m}^2$.

The adhesion hysteresis for PS-g-PEO surfaces measured in air is different from the non-hysteric forces between the polymer surfaces in aqueous solution. As discussed for Figure 0.6, the non-hysteric forces in aqueous solution resulted from the steric interactions of the swollen PEO brushes. The adhesion hysteresis of PS-g-PEO surfaces in air are considered to be mainly due to the interdigitation of polymer chains/segments across the contact interface while the hydrogen bonding between the PEO chains at the polymer-polymer interface can also play a role. [60-62]

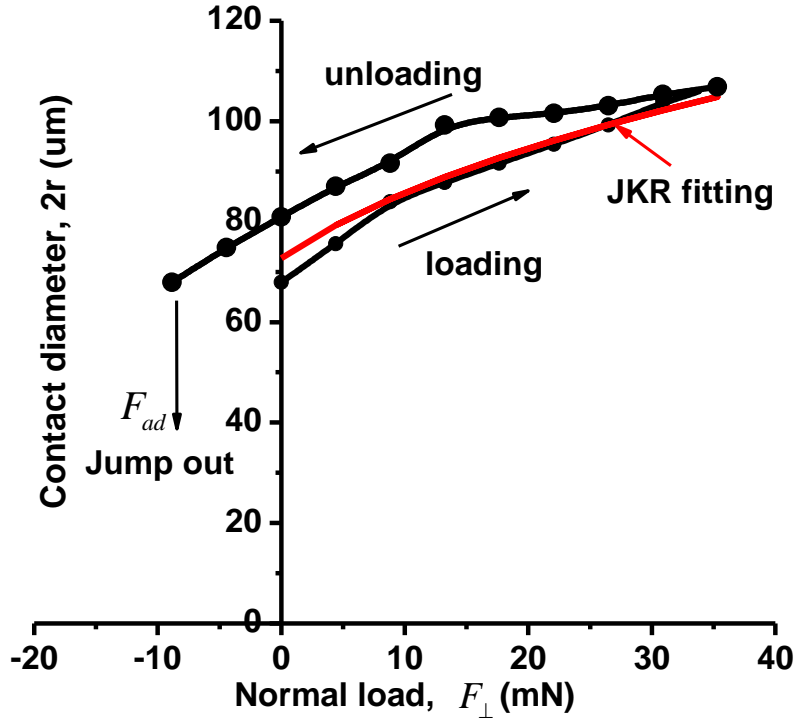


Figure 0.7 Contact diameter $2r$ vs. applied load F_{\perp} obtained through the JKR loading-unloading test for two PS-g-PEO films. Red solid line is the fitted curve for the loading path using the JKR model.

1.13.2 Surface energy by three-probe-liquid contact angle measurement

The surface energy of PS-g-PEO surface was also determined by sessile drop method based on the contact angle measurements of three probe liquids. In the Good & Van Oss model, [40, 41] the surface energy can be written as Equation 9, where γ is the surface energy, γ^d is the dispersive component (Lifshitz-Van der Waals interactions), and γ^+ and γ^- are the polar components (Lewis acid-base).

$$\gamma = \gamma^d + 2\sqrt{\gamma^+ \gamma^-} \quad (9)$$

The relation between liquid contact angle θ , surface tension of liquid, and surface energy components of solid surface and liquid can be given by Equation 10, where L and S represent the liquid and solid phases, respectively.

$$\gamma_L(1 + \cos \theta) = 2\left(\sqrt{\gamma_S^d \gamma_L^d} + \sqrt{\gamma_S^+ \gamma_L^-} + \sqrt{\gamma_L^+ \gamma_S^-}\right) \quad (10)$$

In order to determine the surface energy components of the solid, γ_S^d , γ_S^+ and γ_S^- , at least three different probe liquids of known energy components should be used in contact angle measurements and then three equations can be obtained. Thus, the energy components of the solid surface can be determined by Equation 11, where L1, L2 and L3 denote the three different probe liquids, respectively.

$$\begin{bmatrix} \gamma_S^d \\ \gamma_S^+ \\ \gamma_S^- \end{bmatrix} = \left\{ \left[\begin{array}{ccc} \sqrt{\gamma_{L1}^d} & \sqrt{\gamma_{L1}^-} & \sqrt{\gamma_{L1}^+} \\ \sqrt{\gamma_{L2}^d} & \sqrt{\gamma_{L2}^-} & \sqrt{\gamma_{L2}^+} \\ \sqrt{\gamma_{L3}^d} & \sqrt{\gamma_{L3}^-} & \sqrt{\gamma_{L3}^+} \end{array} \right]^{-1} \begin{pmatrix} \gamma_{L1} [\cos \theta_1 + 1] \\ \gamma_{L2} [\cos \theta_2 + 1] \\ \gamma_{L3} [\cos \theta_3 + 1] \end{pmatrix} \right\}^2 \quad (11)$$

The three probe liquids used in this study were Dimethyl sulfoxide (DMSO), Glycerol and Ethylene glycol, and their surface tension components are given in Table 0.2.

Table 0.2 Three probe liquids for measuring the surface energy of PS-g-PEO film [63].

Liquid	γ_L^d	γ_L^+	γ_L^-	γ_L
Dimethyl sulfoxide	36.0	0.5	32.0	44.0
Glycerol	34.0	3.9	57.4	64.0
Ethylene glycol	29.0	1.9	47.0	48.0

Table 0.3 The contact angles of three probe liquids on PS-g-PEO film.

	Contact angle θ		
	Dimethyl sulfoxide	Glycerol	Ethylene glycol
t=0 s	48.5	80.6	66.3
t=60 s	45.5	75.0	61.1

Table 0.4 The surface energy of PS-g-PEO film.

	γ_s^d	γ_s^+	γ_s^-	γ_s
t=0 s	37.9	0.078	3.1	38.8
t=60 s	38.8	0.2	14.2	42.2

The contact angles of the three different probe liquids on PS-g-PEO surface are shown in Table 0.3. It should be noted that the contact angles of the three

probe liquids on PS-g-PEO all became slightly smaller with time as shown in Table 0.3, but they all reached a static angle within a minute, which indicates that the polymer surface, especially the PEO branches, could have certain conformation rearrangement induced by their molecular interactions with the contacting liquids. The surface energy components of PS-g-PEO film was then calculated by using Equations 11, and the surface energy was determined to be 38.8 mJ/m^2 , which is excellent agreement with the value obtained from the JKR contact mechanics test by SFA. Thus, the surface energy of PS-g-PEO film was determined to be $38.0 \pm 1.0 \text{ mJ/m}^2$. The calculated surface energy of PS-g-PEO film increased slightly to 42.2 mJ/m^2 by using the contact angles at $t=60 \text{ s}$. It is noted that the surface energies reported for PS and PEO are about $34\text{-}40 \text{ mJ/m}^2$ and $41.5\text{-}44.0 \text{ mJ/m}^2$, respectively. [9, 64, 65] Thus, it is evident from the increase of the surface energy that conformation rearrangement of PEO chains occurred at polymer-liquid interfaces as discussed above.

1.14 Conclusion

The surface properties and molecular interactions of comb-type polymer PS-g-PEO were investigated in both NaCl solution and air by using SFA, AFM and contact angle measurements. It is evident from the water contact angle measurement that the PEO branch chains can rearrange their conformations and extend into the aqueous solution due to the strong van de Waals force and hydrogen bonding between hydrophilic PEO segments and water molecules. The change of polymer surface morphology was confirmed by AFM imaging and SFA force measurement. Only pure repulsive forces were detected in both symmetric

(polymer vs. polymer) and asymmetric (polymer vs. mica) configurations in NaCl solutions. The ionic strength of NaCl solution showed negligible effect on the interaction forces of PS-g-PEO films due to the neutral nature of PEO branches. The long-range repulsive forces can be well fitted by the Alexander-de Gennes scaling theory, indicating that the repulsive forces between mica-polymer and polymer-polymer have a steric origin, which mainly arise from the interactions of the neutral swollen PEO brushes in aqueous solutions. The surface energy of PS-g-PEO film was determined to be 38.0 ± 1.0 mJ/m² by both adhesion mechanics test and three-probe liquid contact angle measurement. The PS-g-PEO comb-type copolymer shows good potential in antifouling related applications. As PEO has been found to be promising and widely used in the development of antifouling surfaces, our results on comb-type PS-g-PEO may also provide some insights into fundamental understanding of surface properties and molecular interaction mechanisms of comb-type copolymers and development of functional polymers/coatings with strong antifouling capabilities for important engineering and biomedical applications.

Acknowledgement

This research was supported by a Collaborative Research and Development (CRD) Grant Award from the Natural Sciences and Engineering Research Council of Canada (NSERC) and Teck Metals Ltd. The authors also acknowledge the support of an NSERC Discovery Grant Award and an NSERC RTI Grant Award (for a Surface Forces Apparatus, SFA).

Supplementary Information

X-ray photoelectron spectroscopy (XPS)

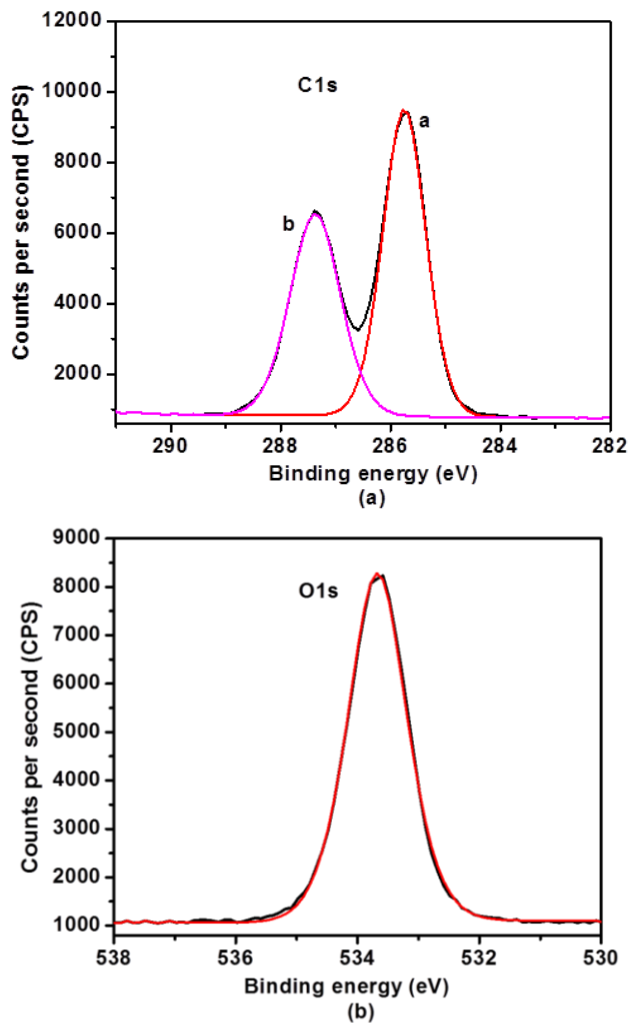


Figure S0.1 High resolution XPS spectrum of spin-coated PS-g-PEO film: (a) C1s spectrum and (b) O1s spectrum.

The XPS analysis shows that the amount of O increased from 15.1 ± 0.2 at% for original spin-coated polymer surface to 16.3 ± 0.2 at% after the surface was treated by water and then dried. Such a small increase (1.2 at%) of O content was most likely due to the conformational rearrangement of PS-g-PEO molecules in

the interfacial layer after the polymer surface was exposed to water and the PEO branches extended into the aqueous phase. It should be also noted that the O content change determined by XPS on polymer surface was rather small after treated by water, much lower than that in PEO chains (~33 at%), which could be caused by two factors: (1) XPS can detect the elements on the top polymer layer of several nm (normally up to ~10 nm) and the element content determined was an average of the whole interfacial layer (not only the upmost surface), and (2) the XPS tests were conducted on dry polymer samples after kept in vacuum for ~25 hrs during which period some of hydrophobic polystyrene units/segments might rearrange and migrate back to surface layer.

Alexander de Gennes (AdG) fitting of force-distance profiles using single set of parameters

Figure S2a and S2b show the fitting of measured repulsive forces of PS-g-PEO films with the AdG theory (solid curves, using single set of fitting parameters) in both symmetric and asymmetric configurations in 1 mM and 100 mM NaCl solutions, respectively. It was found that the fitting by using single set of parameters in the AdG theory (Equations 3 and 4) can only well describe the measured steric forces at long separation distance under low compression and it deviates at short distance under high compression.

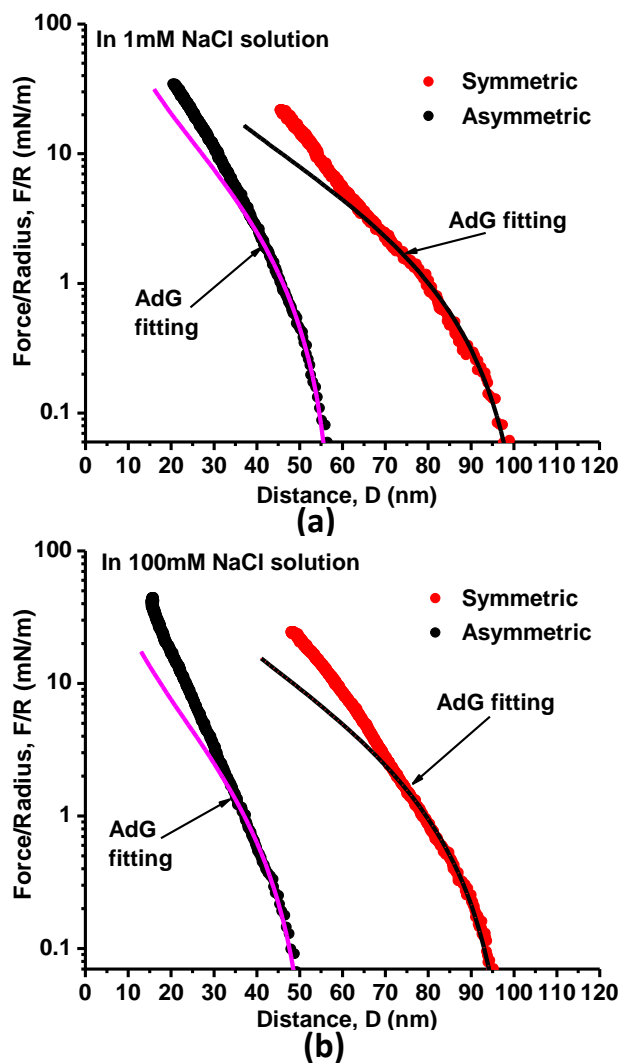


Figure S0.2 Experimentally measured force-distance profiles (dot plots) for PS-g-PEO vs mica (asymmetric configuration) and two PS-g-PEO surfaces (symmetric configuration), and theoretically fitted curves using the AdG theory (using single set of fitting parameters) in (a) 1 mM NaCl and (b) 100 mM NaCl solution.

References

- [1] M.A. Bevan, S.N. Petris, D.Y.C. Chan, *Langmuir*, 18 (2002) 7845.
- [2] M.A. Bevan, D.C. Prieve, *Langmuir*, 16 (2000) 9274.
- [3] R.B. Cheyne, M.G. Moffitt, *Langmuir*, 22 (2006) 8387.
- [4] J.K. Cox, K. Yu, B. Constantine, A. Eisenberg, R.B. Lennox, *Langmuir*, 15 (1999) 7714.
- [5] A.M.G. daSilva, E.J.M. Filipe, J.M.R. dOliveira, J.M.G. Martinho, *Langmuir*, 12 (1996) 6547.
- [6] D. Guzonas, D. Boils, M.L. Hair, *Macromolecules*, 24 (1991) 3383.
- [7] J. Juarez, S. Goy-Lopez, A. Cambon, M.A. Valdez, P. Taboada, V. Mosquera, *J Phys Chem C*, 114 (2010) 15703.
- [8] Y. Li, H.Y. Liu, J.L. Song, O.J. Rojas, J.P. Hinestroza, *Acs Appl Mater Inter*, 3 (2011) 2349.
- [9] C. Neto, M. James, A.M. Telford, *Macromolecules*, 42 (2009) 4801.
- [10] B. Reining, H. Keul, H. Hocker, *Polymer*, 43 (2002) 7145.
- [11] N.V. Salim, Q.P. Guo, *J Phys Chem B*, 115 (2011) 9528.
- [12] D. Scalarone, J. Tata, F. Caldera, M. Lazzari, O. Chiantore, *Mater Chem Phys*, 128 (2011) 166.
- [13] J. Zhang, H.Q. Cao, X.H. Wan, Q.F. Zhou, *Langmuir*, 22 (2006) 6587.
- [14] B.H. Pettersen, L. Bergflodt, J. Sjoblom, *Colloid Surface A*, 127 (1997) 175.

- [15] G.L. Kenausis, J. Voros, D.L. Elbert, N.P. Huang, R. Hofer, L. Ruiz-Taylor, M. Textor, J.A. Hubbell, N.D. Spencer, *J Phys Chem B*, 104 (2000) 3298.
- [16] S. Lee, M. Muller, M. Ratoi-Salagean, J. Voros, S. Pasche, S.M. De Paul, H.A. Spikes, M. Textor, N.D. Spencer, *Tribol Lett*, 15 (2003) 231.
- [17] S.S. Perry, X.P. Yan, F.T. Limpoco, S. Lee, M. Muller, N.D. Spencer, *Acs Appl Mater Inter*, 1 (2009) 1224.
- [18] M.A. Brady, F.T. Limpoco, S.S. Perry, *Langmuir*, 25 (2009) 7443.
- [19] A. Asatekin, S. Kang, M. Elimelech, A.M. Mayes, *J Membrane Sci*, 298 (2007) 136.
- [20] G.N. Njikang, L. Cao, M. Gauthier, *Macromol Chem Phys*, 209 (2008) 907.
- [21] J.N. Israelachvili, G.E. Adams, *J Chem Soc Farad T 1*, 74 (1978) 975.
- [22] J.N. Israelachvili, P.M. McGuiggan, *J Mater Res*, 5 (1990) 2223.
- [23] D. Leckband, J. Israelachvili, *Q Rev Biophys*, 34 (2001) 105.
- [24] T.L. Kuhl, D.E. Leckband, D.D. Lasic, J.N. Israelachvili, *Biophys J*, 66 (1994) 1479.
- [25] H. Zeng, Y. Tian, T.H. Anderson, M. Tirrell, J.N. Israelachvili, *Langmuir*, 24 (2008) 1173.
- [26] Y.J. Min, M. Akbulut, J.R. Sangoro, F. Kremer, R.K. Prud'homme, J. Israelachvili, *J Phys Chem C*, 113 (2009) 16445.
- [27] Y.J. Min, M. Akbulut, N. Belman, Y. Golan, J. Zasadzinski, J. Israelachvili, *Nano Lett*, 8 (2008) 246.

- [28] D.D. Lowrey, K. Tasaka, J.H. Kindt, X. Banquy, N. Belman, Y. Min, N.S. Pesika, G. Mordukhovich, J.N. Israelachvili, *Tribol Lett*, 42 (2011) 117.
- [29] J. Israelachvili, *Intermolecular and Surface Forces*, third ed., Academic Press, 2011.
- [30] J. Israelachvili, Y. Min, M. Akbulut, A. Alig, G. Carver, W. Greene, K. Kristiansen, E. Meyer, N. Pesika, K. Rosenberg, H. Zeng, *Rep Prog Phys*, 73 (2010) 1.
- [31] Q.Y. Lu, J. Wang, A. Faghihnejad, H.B. Zeng, Y. Liu, *Soft Matter*, 7 (2011) 9366.
- [32] A. Natarajan, J.G. Xie, S.Q. Wang, Q.X. Liu, J. Masliyah, H.B. Zeng, Z.H. Xu, *J Phys Chem C*, 115 (2011) 16043.
- [33] F.C. Teng, H.B. Zeng, Q.X. Liu, *J Phys Chem C*, 115 (2011) 17485.
- [34] Israelac.Jn, *J Colloid Interf Sci*, 44 (1973) 259.
- [35] M. Benz, K.J. Rosenberg, E.J. Kramer, J.N. Israelachvili, *J Phys Chem B*, 110 (2006) 11884.
- [36] N.H. Chen, N. Maeda, M. Tirrell, J. Israelachvili, *Macromolecules*, 38 (2005) 3491.
- [37] N. Maeda, N.H. Chen, M. Tirrell, J.N. Israelachvili, *Science*, 297 (2002) 379.
- [38] H.B. Zeng, N. Maeda, N.H. Chen, M. Tirrell, J. Israelachvili, *Macromolecules*, 39 (2006) 2350.
- [39] H.B. Zeng, M. Tirrell, J. Israelachvili, *J Adhesion*, 82 (2006) 933.

- [40] C.J. Vanoss, *Colloid Surface A*, 78 (1993) 1.
- [41] C.J. Vanoss, R.J. Good, M.K. Chaudhury, *J Colloid Interf Sci*, 111 (1986) 378.
- [42] R. Gunawidjaja, S. Peleshanko, K.L. Genson, C. Tsitsilianis, V.V. Tsukruk, *Langmuir*, 22 (2006) 6168.
- [43] I. Lynch, L. Piculell, *J Phys Chem B*, 108 (2004) 7515.
- [44] I.I. Perepichka, A. Badia, C.G. Bazuin, *Acs Nano*, 4 (2010) 6825.
- [45] E.W. Price, S. Harirchian-Saei, M.G. Moffitt, *Langmuir*, 27 (2011) 1364.
- [46] S.L. McGurk, R.J. Green, G.H.W. Sanders, M.C. Davies, C.J. Roberts, S.J.B. Tendler, P.M. Williams, *Langmuir*, 15 (1999) 5136.
- [47] T. Pettersson, A. Naderi, R. Makuska, P.M. Claesson, *Langmuir*, 24 (2008) 3336.
- [48] U. Raviv, J. Frey, R. Sak, P. Laurat, R. Tadmor, J. Klein, *Langmuir*, 18 (2002) 7482.
- [49] S.R. Sheth, D. Leckband, *P Natl Acad Sci USA*, 94 (1997) 8399.
- [50] J. Israelachvili, *P Natl Acad Sci USA*, 94 (1997) 8378.
- [51] M.M. Coleman, *Fundamentals of Polymer Science: An Introductory Text*, Second Edition, CRC Press, 1998.
- [52] P.G. Degennes, *Adv Colloid Interfac*, 27 (1987) 189.
- [53] M. Akbulut, A.R.G. Alig, Y. Min, N. Belman, M. Reynolds, Y. Golan, J. Israelachvili, *Langmuir*, 23 (2007) 3961.

- [54] K.L. Johnson, K. Kendall, A.D. Roberts, Proc R Soc Lon Ser-A, 324 (1971) 301.
- [55] B.X. Zhao, N. Pesika, K. Rosenberg, Y. Tian, H.B. Zeng, P. McGuiggan, K. Autumn, J. Israelachvili, Langmuir, 24 (2008) 1517.
- [56] H.B. Zeng, N. Pesika, Y. Tian, B.X. Zhao, Y.F. Chen, M. Tirrell, K.L. Turner, J.N. Israelachvili, Langmuir, 25 (2009) 7486.
- [57] B. Benli, J. Nalaskowski, S. Assemi, M.S. Celik, J.D. Miller, J Adhes Sci Technol, 25 (2011) 1159.
- [58] F.P. Bowden, Tabor, D., The friction and lubrication of solids, Clarendon Press, Oxford, 1986.
- [59] K.L. Johnson, Contact mechanics, Cambridge University Press, Cambridge Cambridgeshire, New York, 1985.
- [60] M. Deruelle, M. Tirrell, Y. Marciano, H. Hervet, L. Leger, Faraday Discuss, 98 (1994) 55.
- [61] M. Aubouy, L. Leger, Y. Marciano, E. Raphael, H.R. Brown, Aip Conf Proc, (1996) 3.
- [62] M. Deruelle, L. Leger, M. Tirrell, Macromolecules, 28 (1995) 7419.
- [63] M. Rankl, S. Laib, S. Seeger, Colloid Surface B, 30 (2003) 177.
- [64] T. Ghoshal, M.T. Shaw, C.T. Bolger, J.D. Holmes, M.A. Morris, J Mater Chem, 22 (2012) 12083.
- [65] M. Tirrell, Langmuir, 12 (1996) 4548.

CHAPTER 4 EFFECT OF POLYCARBOXYLATE ETHER COMB-TYPE POLYMER ON VISCOSITY AND INTERFACIAL PROPERTIES OF KAOLINITE CLAY SUSPENSION²

1.15 Introduction

The viscosity and interfacial properties of clay mineral suspensions are important for many engineering and industrial applications including processing of ceramics, manufacture of cements, formulation of inks and paints, production of pulp and paper, transportation of coal [1] and flotation of minerals. [2, 3] For instance, industrial waste residues known as tailings contain a large amount of clay particles. The treatment of such waste residues has been a major challenge for decades in coal, mineral processing and oil sands industry. Extensive research has been conducted to understand the interfacial properties and interactions between flocculants and clay particles in the context of investigating the flocculation of clay suspensions for tailings treatment. [4-8] On one hand, fine clay particles disperse well and will retard the settling performance of mineral tailings. On the other hand, clay can also self-aggregate in pigment for paper coating and in cementitious system. In paper coatings, the pigment content can be as high as 60-70% and efficient dispersants are normally needed to stabilize the pigment suspension. [9] In cement, clay particles have a significant impact on its

² A version of this chapter has been published. L. Zhang, Q. Lu, Z. Xu, Q. Liu, H. Zeng 2012. Journal of Colloid and Interface Science. 378: 222–231.

rheological properties, reducing the fluidity of cement and leading to higher water consumption in order to maintain appropriate workability of cement. Therefore, a polymeric modifier is often used to reduce the water content of cement and to retain its workability when large quantities of industrial wastes such as slag and fly ash were present in the concrete mixture. [10-12]

Polymer additives have been widely used in various colloidal suspensions to either stabilize or flocculate the colloidal particles, depending on the purpose of applications. Comb type polymers have been shown to be effective additives in stabilizing different colloidal systems. [4, 13-22] In cement industry, for example, the comb type polymer, polycarboxylate ethers (PCEs), has been commonly used to control the stability and rheology of process streams and known as superplasticizers or water-reducing admixtures. The addition of this comb type polymer PCE to fresh concrete can impact the interfacial properties between particles and liquid medium, controlling the bulk physical properties (i.e., viscosity) of suspensions and reducing water to cement ratio of the hardened paste. [22-25] The dispersing effect of PCE is suggested to be mainly due to the adsorption of these polymers on particle surfaces, which induces electrostatic and/or steric repulsive forces among the particles. [26] The comb type polymer PCE consists of a negatively charged backbone and neutral polyethylene-oxide (PEO) side chains, as illustrated in Figure 0.1. Both the length and number of side chains can be varied to manipulate the adsorption behaviour of PCEs and their ability to control the stability of dispersions. Although great efforts have been devoted to investigating the interaction mechanisms between various polymer surfaces,

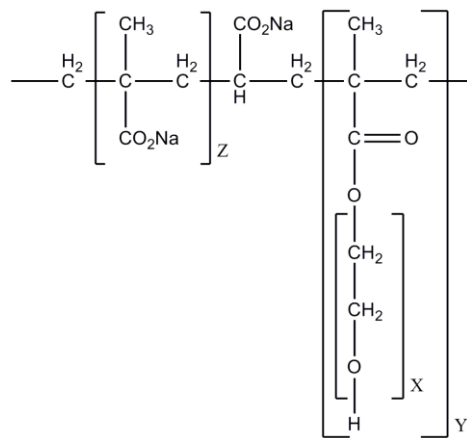
brushes and thin films using different techniques including atomic force microscope (AFM) and surface forces apparatus (SFA), [27-35] few study is available on the interactions in clay suspensions containing comb-type polymers.

In this work, kaolinite clay particles were chosen as a model system, due to its wide range of applications in many industrial processes and products, to investigate the effects of PCE on the viscosity and interfacial properties of the kaolinite suspensions. Combined with settling tests, various fundamental measurements including viscosity, zeta potential and surface forces provide complementary information regarding the interactions between PCE and kaolinite particles, and their consequences on stability of kaolinite suspensions. The results obtained in this study provide an insight into the basic interaction mechanisms between clay particles and polymer additives in many colloidal suspensions, which is of both practical and fundamental importance.

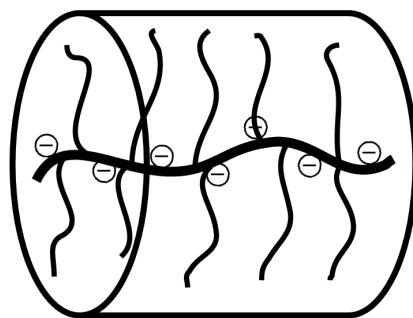
1.16 Materials

The kaolinite clay used in this project was purchased from Kentucky Tennessee Clay Co. The particle size distribution was determined with a MasterSizer 2000 to be $D_{90}=19.38 \mu\text{m}$, $D_{50}=4.69 \mu\text{m}$ and $D_{10}=0.16 \mu\text{m}$. $D_{90}=19.38 \mu\text{m}$ means that the mean diameter of 90 wt% particles is below 19.38 μm . $D_{50}=4.69 \mu\text{m}$ and $D_{10}=0.16 \mu\text{m}$ suggest that the mean diameter of over 50 wt% and 10wt% of particles is below 4.69 μm and 0.16 μm , respectively. Aqueous solutions were prepared in 18.2 M Ω cm deionized water (Millipore, Mississauga, ON, Canada). PCE Melflux 2651F provided by BASF (Germany) was used as

received. The chemical structure and schematic conformation of PCE are shown in Figure 0.1.



(a)



(b)

Figure 0.1 (a) Chemical structure and (b) schematic structure (brush conformation) of a super-plasticizer, PCE used in this work

1.17 Experimental Methods

1.17.1 Sample preparation

Clay suspension was prepared by mixing kaolinite particles with the DI water. A given amount of clay particles were added slowly into the DI water under constant stirring until a desired solid concentration was reached. PCE

solutions of different concentrations were then added by following the same procedure. In this work, the “PCE dosage” in this study refers to the mass percent of PCE to kaolinite, i.e., the same as “polymer/kaolinite mass ratio”.

1.17.2 Viscosity measurement

Viscosity was measured using a concentric cylinder with the standard vane rotor on a TA Instruments AR G2 rheometer. A thermal jacket was used to control the temperature of suspension samples at 25 C° . About 25ml clay suspension was required for each measurement. During the measurement, each sample was pre-sheared for 2 min at a shear rate of 10 s^{-1} and then the measurement was conducted at $10\text{--}1000\text{ s}^{-1}$. The viscosity of kaolinite suspensions (μ) was determined as a function of shear rate ($\dot{\gamma}$) at pH=3.4 and pH=8.3. The pH of the suspension was adjusted by sodium hydroxide stock solutions.

1.17.3 Zeta potential measurement

Zeta potential of kaolinite suspension was measured using a ZetaPALS instrument (Brookhaven Instrument Corporation, USA). Kaolinite suspensions of 2 wt% solids with different PCE dosages were prepared at both pH=3.4 and pH=8.3, in which the PCE dosages were kept the same as that used in the viscosity measurement. The clay suspension was allowed to settle for 24 hours before the supernatant was taken for zeta potential measurement. All the measurements were conducted at 25 C° .

1.17.4 Settling tests

Kaolinite suspension of 2 wt% solids was prepared and mixed for 24 hours to ensure that the kaolinite suspension was well dispersed. The prepared suspensions were then transferred to 100 ml-graduated cylinders for settling tests. Time required for the mud line (the solid-liquid interface) to descend by every 10 ml was recorded. The settling curve was constructed by plotting the normalized mud-line height (h/H) as a function of time, where H and h were the initial height of suspension and the height of the mud line at specified time, respectively. The initial settling rate (ISR) was obtained from the initial slope of the settling curve.

1.17.5 Measurement of interaction force using Surface Forces Apparatus

Interaction forces as a function of separation distance (D) between two mica surfaces (model clay surfaces) in PCE solutions were determined using a surface forces apparatus (SFA). The detailed setup for SFA experiments has been reported elsewhere. [36-40] Briefly, two thin mica sheets (1–5 μm) were glued onto cylindrical silica disks of radius $R = 2$ cm. The two silica disks were mounted in the SFA chamber in a crossed-cylinder configuration which was locally equivalent to a sphere of radius R interacting with a flat surface or two spheres of radius $2R$ when the surface separation D was much smaller than R . In SFA experiments, the absolute surface separation (D) was determined in real-time using fringes of equal chromatic order (FECO) in a multiple beam interferometry. [41, 42] In this study, the reference distance ($D = 0$) was determined at the adhesive contact between the two bare mica surfaces in air.

1.18 Results and discussion

1.18.1 Impact of pH on viscosity of kaolinite suspensions

The effect of pH on the viscosity of 35 wt% kaolinite suspension is shown in Figure 0.2. At both pH=3.4 and 8.3, the viscosity of kaolinite suspension shows a shear thinning behaviour, e.g., the viscosity decreases with increasing shear rate. At a shear rate of e.g., 10 s^{-1} , the viscosity of kaolinite suspension at pH=3.4 is almost two orders of magnitude higher than that at pH=8.3. The viscosity decreases significantly from ~ 2.0 to $< 0.1 \text{ Pa}\cdot\text{s}$ at pH=3.4, while it decreases only slightly from 0.03 to 0.01 Pa·s at pH=8.3 when the shear rate increases from 10 to 1000 s^{-1} , indicating kaolinite suspension is highly aggregated at pH=3.4 and well dispersed at pH=8.3.

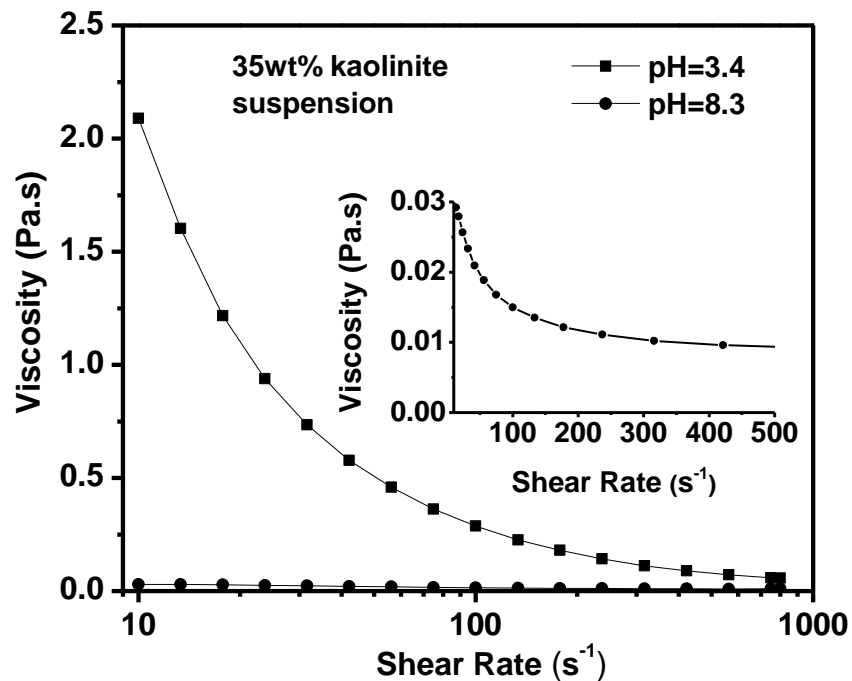


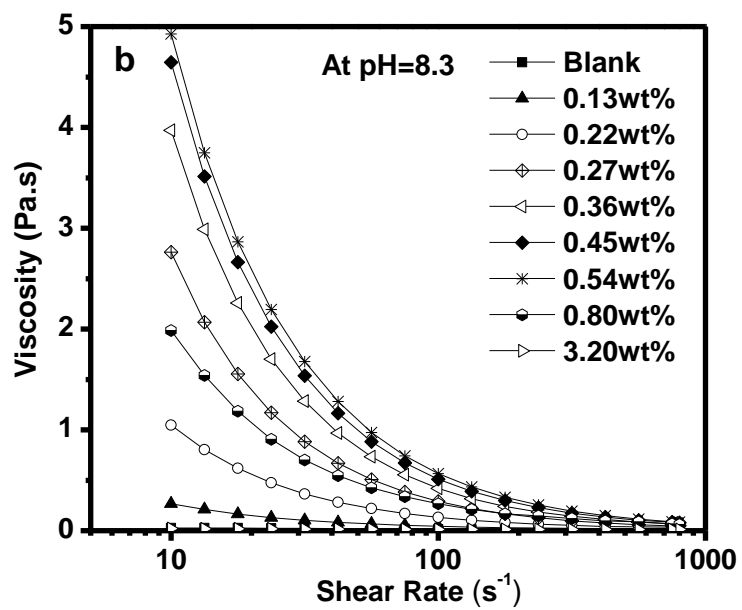
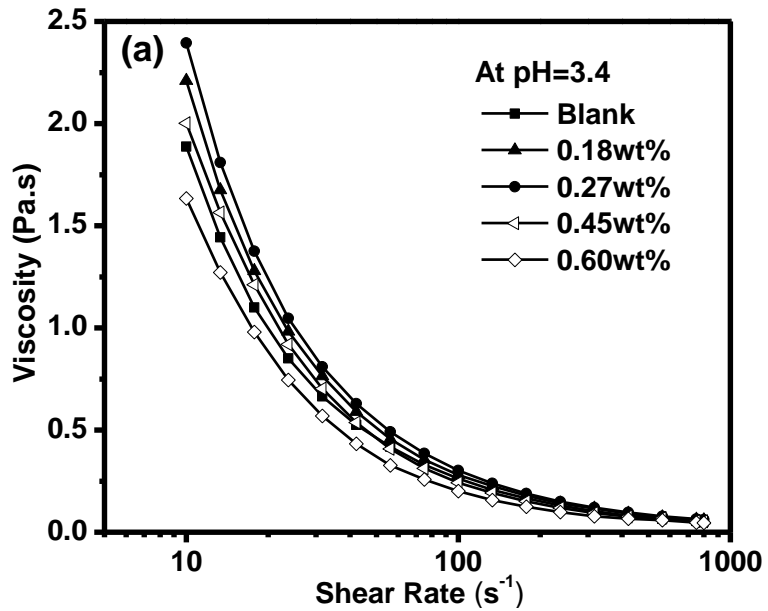
Figure 0.2 Impact of pH on the viscosity of 35 wt% kaolinite suspension. The inset is an expanded drawing of viscosity curve at pH=8.3

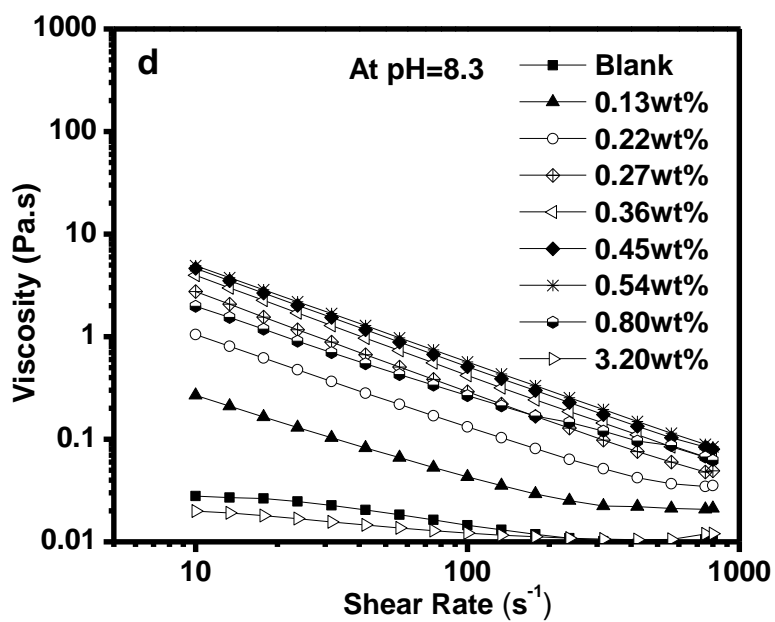
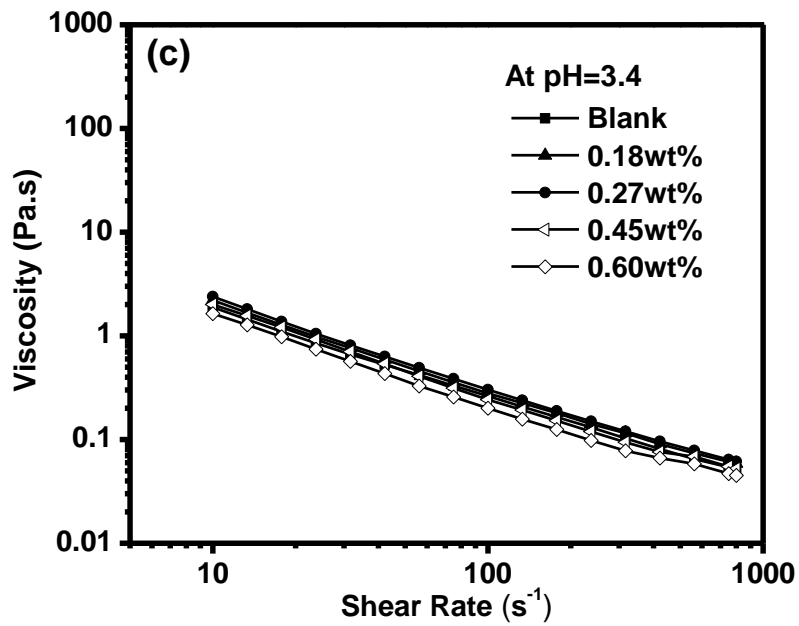
The kaolinite clay consists of a silica tetrahedral layer and an aluminium hydroxide octahedral layer on the basal plane surface. The edge surfaces of kaolinite clay consist of both broken aluminium-oxygen and silicon-oxygen bonds. It is traditionally believed that kaolinite clay carries a permanent negative charge on the basal planes due to isomorphic substitution of Al^{3+} for Si^{4+} in the silica tetrahedral, and $\text{Mg}^{2+}/\text{Fe}^{2+}$ for Al^{3+} in the alumina octahedral layer, which is commonly assumed to be pH-independent, while edge surfaces can carry positive or negative charges depending on the pH of the system. [42] It was also proposed by van Olphen that at pH lower than the isoelectric point of kaolinite particles, there is an electrostatic attraction between positively charged edge surfaces and negatively charged basal planes, showing a high apparent viscosity. [43] In a recent report by Gupta *et al.*, [44] the results of the AFM measurement showed that the charge of kaolinite basal plane is also pH-dependent. The isoelectric point of silica tetrahedral face of the kaolinite was determined at $\text{pH} < 4$, and the isoelectric point of aluminium hydroxide octahedral face between $\text{pH} = 6$ and 8. In our case, it is concluded that the kaolinite particles under acidic condition can self-aggregate through the electrostatic attraction between negatively charged basal planes and positively charged edge edge surfaces, which leads to a high viscosity. In alkaline solutions, both basal planes and edge surfaces are negatively charged, resulting in strong electrostatic repulsion between the kaolinite particles, and therefore low viscosity of the clay suspension.

1.18.2 Effect of PCE on viscosity of kaolinite suspension

The viscosity of kaolinite suspension as a function of shear rate, pH and PCE dosages was determined to understand the interactions between PCE molecules with kaolinite surfaces.

The kaolinite-PCE suspension shows shear thinning behaviour over the whole range of shear rates studied ($10\text{-}1000\text{ s}^{-1}$) as evident in the plots of viscosity vs. shear rate in Figure 0.3a, Figure 0.3b (linear plots) and Figure 0.3c, Figure 0.3d (log-log plots). The viscosity of kaolinite-PCE suspension follows a power law relation with shear rate as $\eta \propto \dot{\gamma}^m$. The best fitted exponents are summarized in Table 0.1. It is evident that the kaolinite-PCE suspensions behave as non-Newtonian fluids. It is interesting to note that at pH=3.4 the exponents m are almost the same at $m = -0.83$. However, at pH=8.3, the exponent m shifts from -0.3 to -0.9 and then from -0.9 to -0.14. The m remains at -0.8 to -0.9 for PCE dosages of 0.22 - 0.54 wt%, which is close to the exponent value obtained at pH=3.4. For kaolinite suspensions with high PCE dosages at pH=8.3, the exponent m increases to -0.14, indicating that the suspension is approaching to a more Newtonian-like fluid.





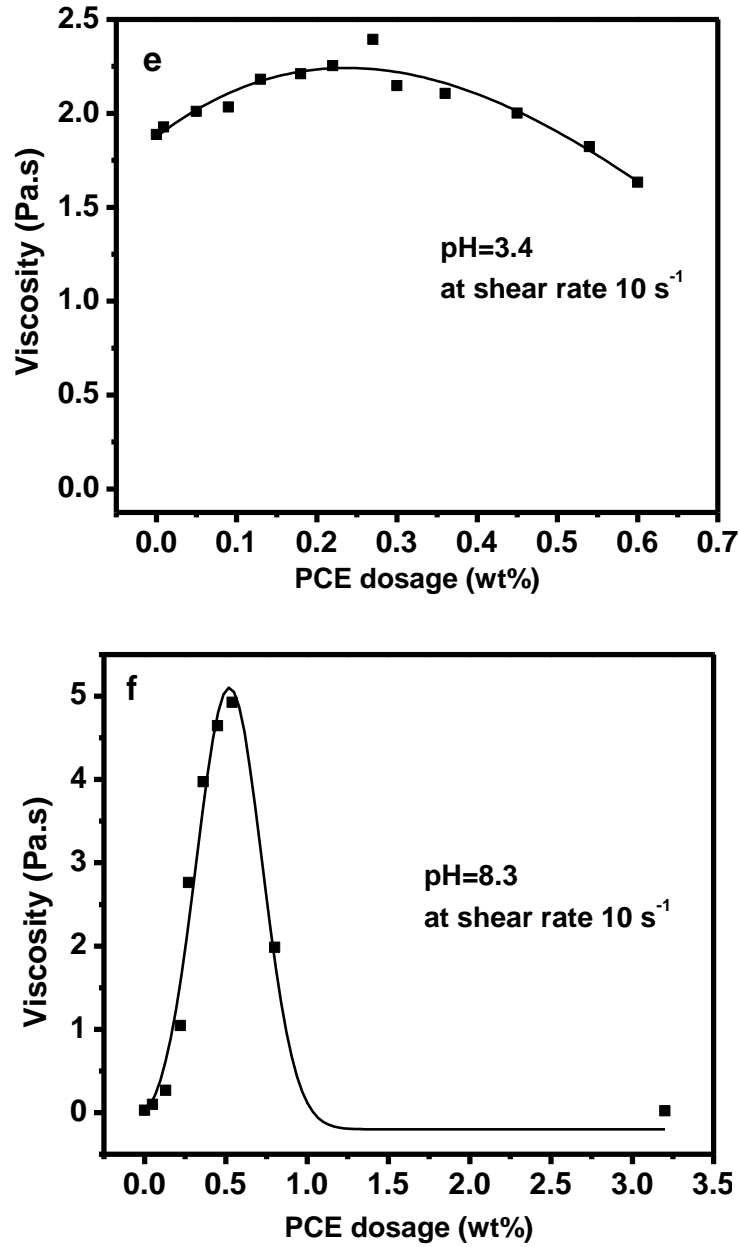


Figure 0.3 Effect of different PCE dosages on the viscosity of 35 wt% kaolinite suspension. Variation of viscosity as a function of shear rate at (a, c) pH=3.4 and (b, d) pH=8.3 in linear plots (a, b) and log-log plots (c, d). The viscosity changes of 35 wt% kaolinite suspension with different PCE dosages at shear rate 10 s^{-1} at (e) pH=3.4 and (f) pH=8.3.

Table 0.1 Power law exponents m in $\eta \propto \dot{\gamma}^m$ for kaolinite suspensions with different PCE dosages at pH=3.4 and 8.3.

Power law exponents m in $\eta \propto \dot{\gamma}^m$											
PCE dosage (wt%)	0	0.13	0.18	0.22	0.27	0.36	0.45	0.54	0.60	0.80	3.20
pH=3.4	-0.82	--	-0.83	--	-0.83	--	-0.84	--	-0.83	--	--
pH=8.3	-0.3	-0.6	--	-0.8	-0.9	-0.9	-0.9	-0.9	--	-0.7	-0.14

The results in Figure 0.3e and Figure 0.3f show that at the shear rate of 10 s^{-1} , the addition of PCE has a marginal impact on the viscosity of kaolinite suspension at pH=3.4, but significantly increases the suspension viscosity by over 100 times at pH=8.3 and 0.5 wt% PCE. For both pH=3.4 and 8.3, the viscosity of kaolinite suspension first increases and then decreases as the PCE dosage increases, and it drops back to (or below) the viscosity of the control (blank) sample at high PCE dosage of ~0.60 wt% and ~3.20 wt% as shown in Figure 0.3e (pH=3.4) and Figure 0.3f (pH=8.3), respectively. The local maximum viscosity occurs at PCE dosage of 0.27 wt% and 0.54 wt% at pH=3.4 and 8.3 respectively.

Yield stress can be used as a single parameter to describe the fluidity of a colloidal suspension. Casson equation, shown in Equation 1 which has been widely applied to many kinds of colloidal suspensions, [45, 46] can be employed here to determine the yield stress of kaolinite suspensions [6]

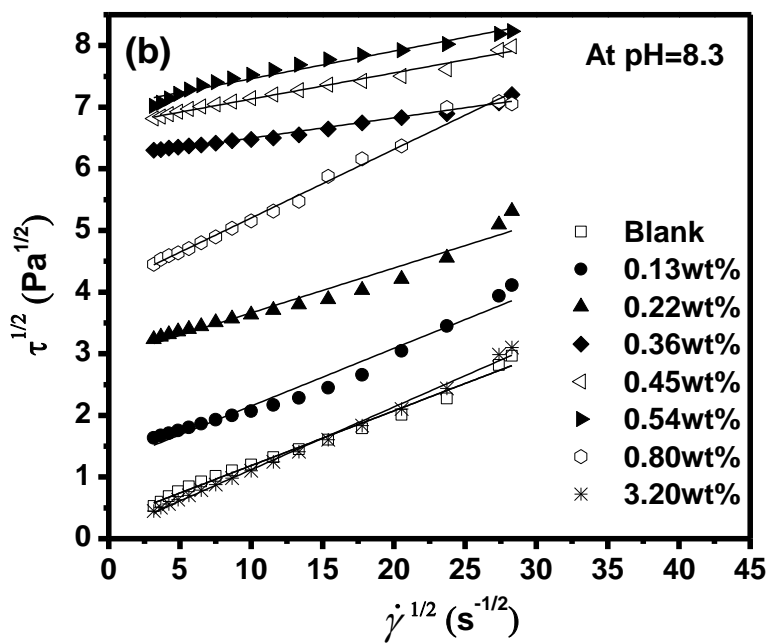
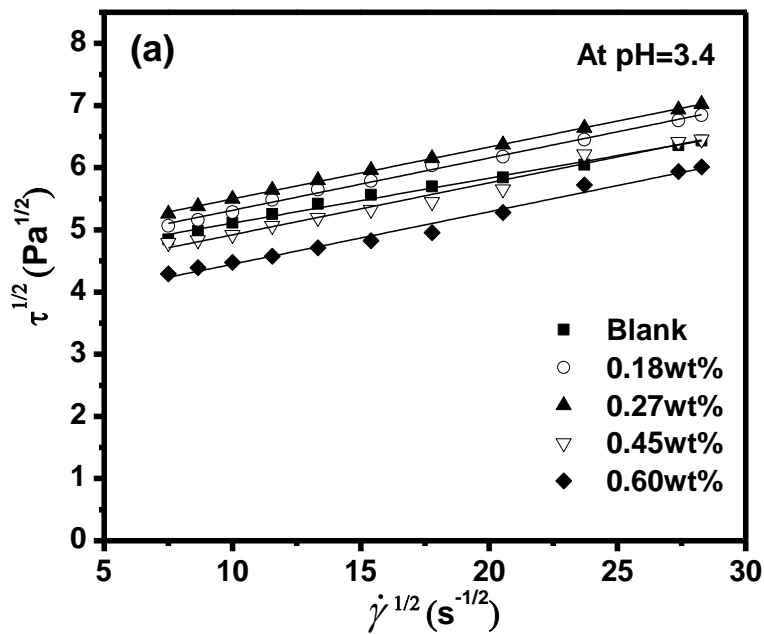
$$\sqrt{\tau} = \sqrt{\tau_c} + \sqrt{\eta_c \dot{\gamma}} \quad , \quad (1)$$

where $\dot{\gamma}$ is the shear rate, τ is the shear stress of the suspension, τ_c and η_c are the Casson yield stress and Casson viscosity, respectively. We can determine τ_c by extrapolating the fitted curve $\sqrt{\tau} \propto \sqrt{\dot{\gamma}}$ to $\dot{\gamma} \rightarrow 0$.

Figure 0.4a and Figure 0.4b show a linear relationship between the square roots of shear stress $\sqrt{\tau}$ and shear rate $\sqrt{\dot{\gamma}}$, indicating that the Casson equation is valid here and can be applied to determine the yield stress of kaolinite suspensions as shown in Figure 0.4c and Figure 0.4d. The maximum yield stress was obtained at the same PCE dosage as that we obtain the maximum viscosity, indicating that kaolinite suspension has the lowest fluidity at PCE dosage of ~ 0.27 wt% and ~ 0.54 wt% for pH=3.4 and 8.3, respectively. The normalized increment of viscosity $(\eta_{PCE} - \eta_{Control}) / \eta_{Control}$ of 35 wt% kaolinite suspension with a PCE dosage of 0.27 wt% under different shear rates is shown in Figure 0.5, which clearly indicates that the increase of suspension viscosity due to the presence of PCE is hundreds of times higher at pH=8.3 than that at pH=3.4.

The viscosity of pure PCE in water with the same dosages as that in the above kaolinite-PCE suspension was measured at pH=3.4 and 8.3, which was 0.001-0.002 Pa•s under shear rates between 10-1000 s^{-1} , which is almost the same as the viscosity of water. It was also found that the addition of PCE had negligible impact on the pH of kaolinite suspension, as shown in Figure 0.6. The above results indicate that the dramatic increase in viscosity with the addition of PCE

polymers at pH=8.3 is due to the interactions between PCE molecules and kaolinite surfaces.



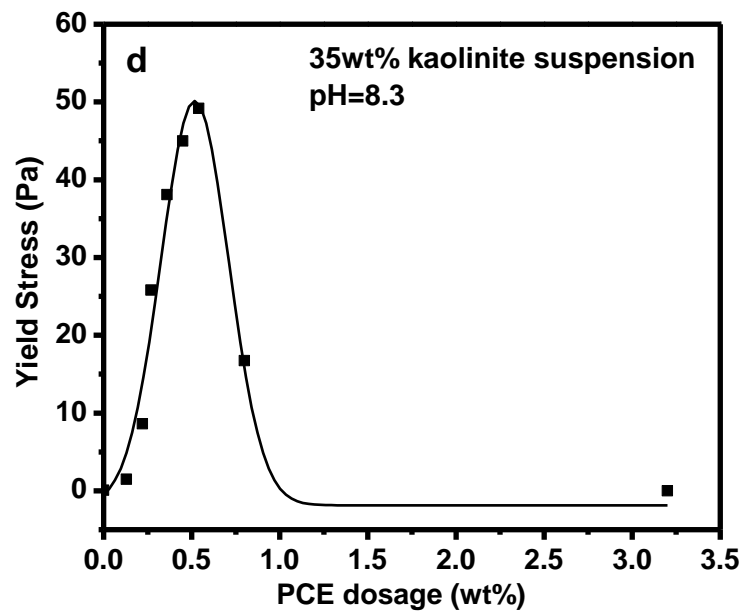
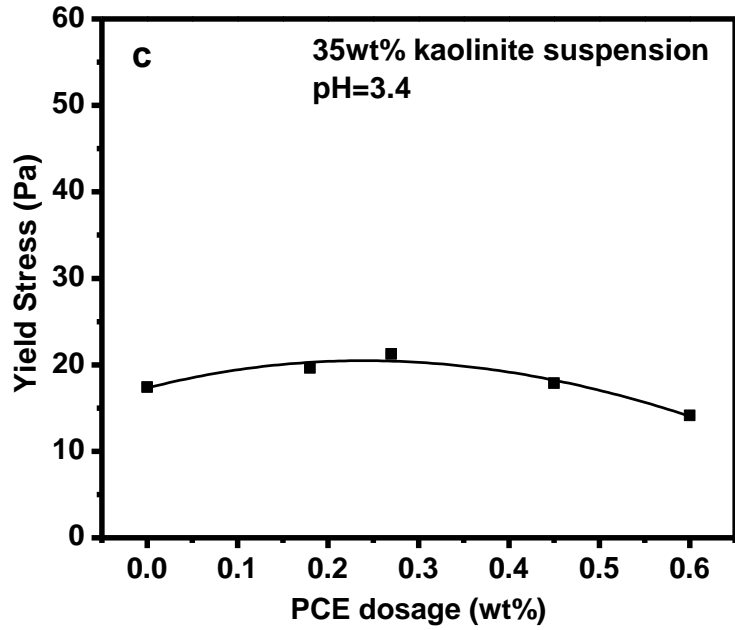


Figure 0.4 The square root of shear stress as a function of square root of shear rate at (a) pH=3.4 and (b) pH=8.3. The yield stress of 35wt% kaolinite suspension with different PCE dosages at (c) pH=3.4 and (d) pH=8.3

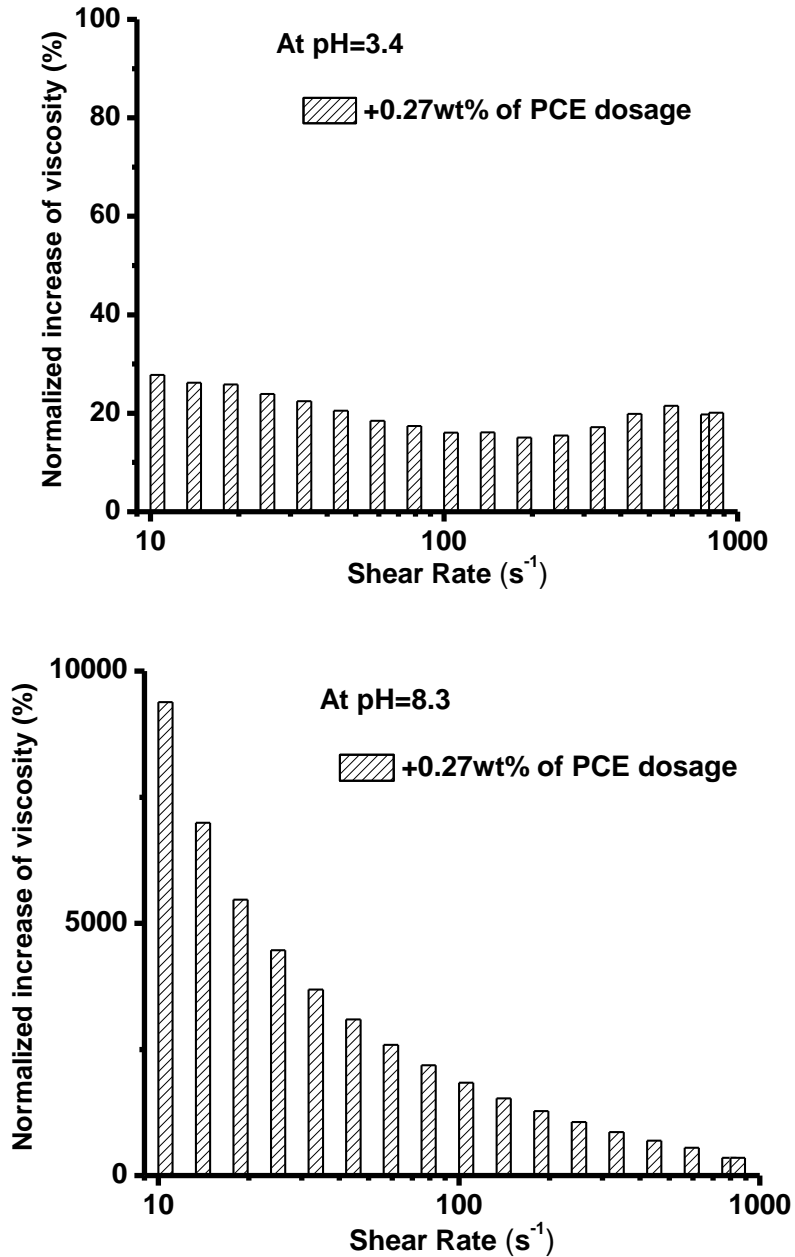


Figure 0.5 The normalized increase of the viscosity of 35 wt% kaolinite suspension with 0.27 wt% of PCE dosage at pH=3.4 and pH=8.3

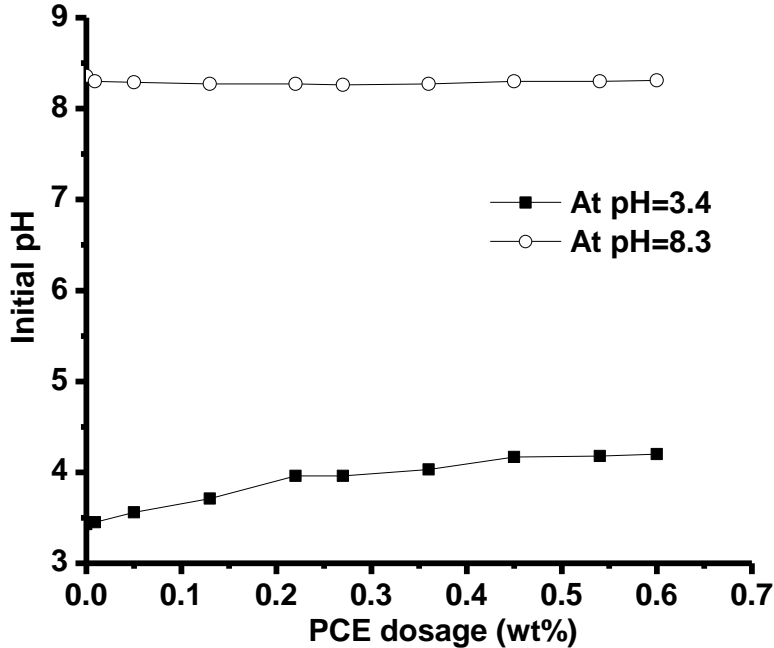


Figure 0.6 The impact of different PCE dosages on the pH of 35wt% kaolinite suspension

1.18.3 Settling tests

The stability of the kaolinite suspensions with and without PCE was investigated by settling tests. Figure 0.7a shows the normalized height h/H of the mud line as a function of settling time in the presence of various PCE dosages at pH=3.4 and 8.3. With low PCE dosage (~ 0.05 wt%) at pH=3.4, the suspension settled slightly faster than that without PCE. However, the suspension hardly settled at high PCE dosage (≥ 0.40 wt%) under pH=3.4 as well as at almost any PCE dosage under pH=8.3. The initial settling rate (ISR) was obtained from the initial slope of the settling curve, and Figure 0.7b shows the ISR as a function of PCE dosage at pH=3.4, which first increases with the PCE dosage and then decreases to almost zero at high dosages. The real-time pictures for the settling of

2 wt% kaolinite suspensions in the presence of 0, 0.05 wt% and 0.40 wt% PCE dosages at pH=3.4 for t=0, 2 and 5 minutes are also shown in Figure 0.8. The above results indicate that under alkaline conditions PCE polymer is always a good dispersant for kaolinite suspension, while under acidic condition it acts as a good dispersant only at high dosages.

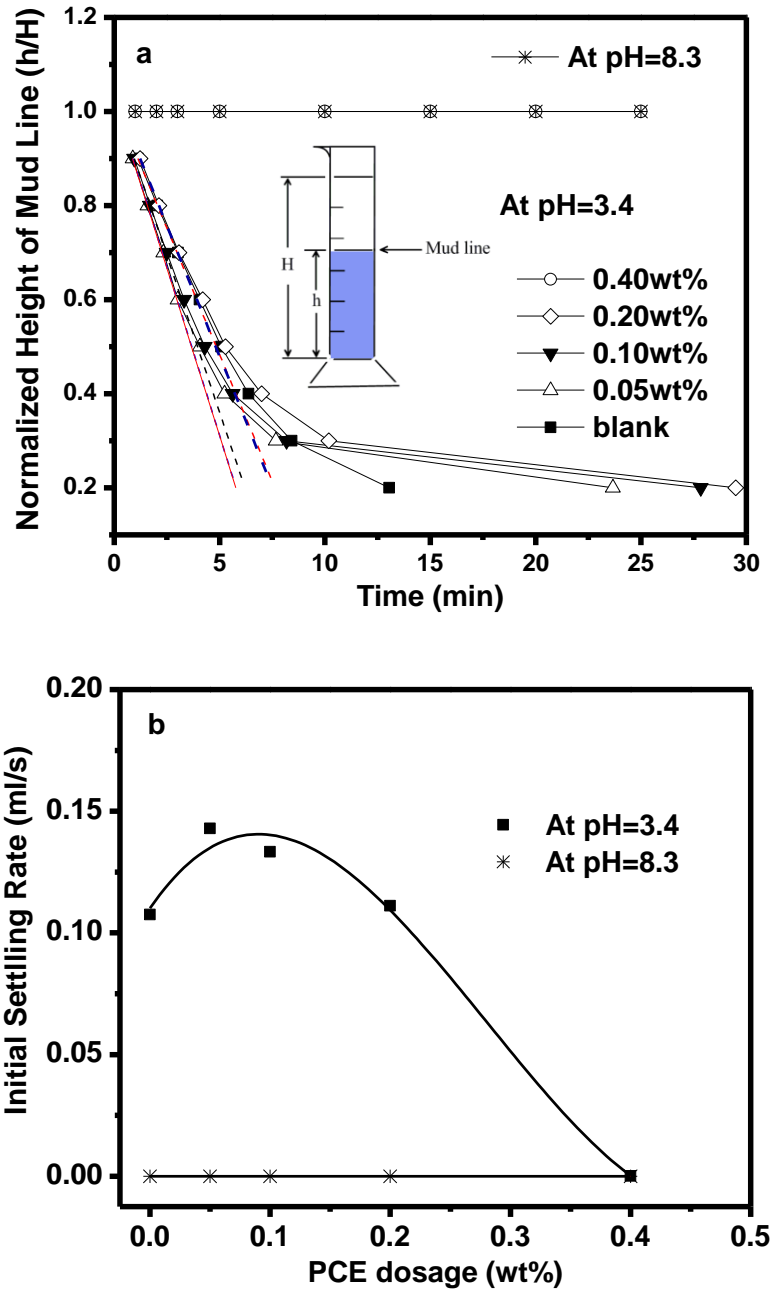


Figure 0.7 (a) The normalized height of mud line as a function of settling time with different PCE dosages; (b) the initial settling rate as a function of PCE dosages at pH=3.4 and 8.3 (Note: a volume settling rate of 1 ml/s corresponds to 1.8 mm/s for the 100 ml-graduated cylinders used here).

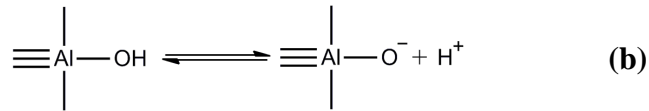
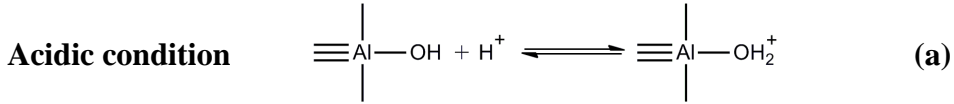


Figure 0.8 Real-time pictures for the settling of 2 wt% kaolinite suspensions at pH=3.4 for t=0, 2 and 5 minutes. Note: samples 1, 2 and 3 contain 0, 0.05 wt% and 0.40 wt% of PCE respectively

1.18.4 Interactions between kaolinite clay particles and PCE polymer

It has been suggested [47-49] that under acidic conditions the aluminol groups on the edge surfaces of kaolinite can be protonated which makes the edge surfaces overall positively charged (shown in reaction a). It has been also reported that at pH=4 the silanol groups would not be protonated which were considered as “free” silanols. Under alkaline condition both aluminol and silanol group can be deprotonated, therefore the edge surface carries negative charge (shown in reaction b and c), whereas the deprotonation of aluminol groups can be neglected (at $\text{pH} \geq 10$) due to the very different p.z.c of alumina and silica (2 for silica and 9 for alumina) and the aluminol groups can be considered “free”. For the PCE used in this study, the polymer chains remain neutral in acidic media. Under alkaline solutions, the carboxylate groups on PCE can be deprotonated which causes the backbones to be negatively charged and fully stretched. Therefore, PCE molecules can interact with kaolinite surfaces via hydrogen bonding from the

PEO side chains and/or electrostatic interaction from the backbones depending on solution conditions.



Alkaline condition



Effects of pH on the interaction mechanism

At pH=3.4, the edge surfaces of kaolinite particles are positively charged (aluminol groups are protonated) which can interact with the negatively charged basal planes, thus the particles can self-aggregate and form clay aggregates as shown in the microscopic images in Figure 0.9a, which leads to a higher viscosity than that in alkaline solutions. At pH=3.4, the addition of PCE shows weak impact on the viscosity of kaolinite suspension. It is proposed that the PCE molecules are able to interact with the kaolinite surface via hydrogen bonding between the PEO side chains and “free” silanol groups, which bring the relatively

clay aggregates in Figure 0.9a together and form larger kaolinite agglomerates as shown in the microscopic image of Figure 0.9b.

At pH=8.3, the kaolinite particles are well dispersed due to electrostatic repulsion between negatively charged basal planes and edge surfaces as shown in Figure 0.9c, and no significant aggregates were observed after the addition of PCE as shown in Figure 0.9d.

Hommer [50] investigated the interactions between PCE and silica, and reported that PCE molecules can be stretched in the aqueous solution due to the repulsion force between both negatively charged silica particles and polymer backbone. Under alkaline condition, the side chains can interact with the silica particles and the PCE molecules adopt a brush-like conformation. In the present study, at pH=8.3, the viscosities of kaolinite suspension showed hundreds of times difference at low and high dosages of PCE, which indicates that at pH=8.3 the interactions between PCE and kaolinite surface would be similar to the silica case reported by Hommer. [50] The interaction between PCE and clay surfaces was further investigated by zeta potential measurement and surface force measurement.

Zeta potential of kaolinite particles in the presence of different PCE dosages at both pH=3.4 and 8.3 is shown in Figure 0.10. It should be noted that the zeta potential measurement was made mainly on the fine particles, i.e., supernatant of clay suspension after settling, as mentioned in Experimental Methods. The point of zero charge (pzc) of kaolinite particles was reported to be about pH=2~3. [51, 52] Therefore, the zeta potential of kaolinite particles measured in this study were both negative at pH=3.4 (-20 mV) and pH=8.3 (-55 mV) in the absence of PCE.

The zeta potential of clay particles does not change with the addition of PCE, which indicates that the PCE molecules do not affect the surface charges of clay particles and they interact with the clay surfaces mainly due to hydrogen bonding via the neutral PEO side chains. The ionization of PCE is mainly due to the ionization of carboxylate groups on the polymer backbone, and the zeta potential of PCE would be similar to that of sodium polymethacrylate. Previous research showed that the zeta potential of sodium polymethacrylate is about -20mV at pH=3 and -50mV at pH=8, [53] which almost overlaps with the zeta potential of kaolinite particles measured at pH=3.4 and pH=8.3. Therefore, the addition of PCE molecules does not show significant impact on the zeta potential of kaolinite particles measured. The interaction forces were further determined using a SFA.

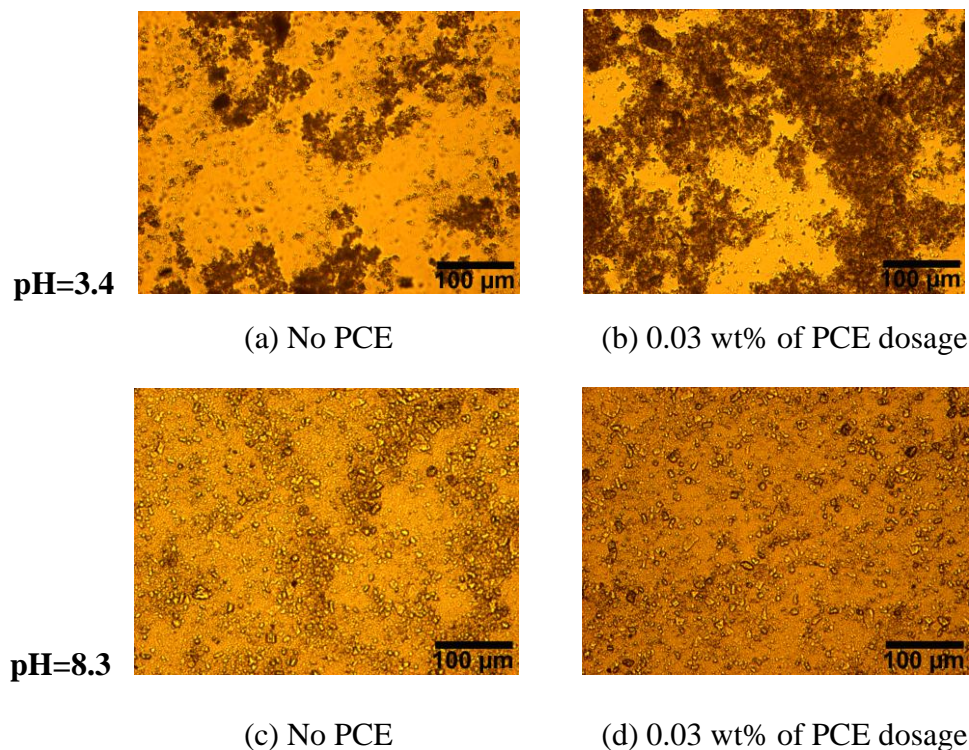


Figure 0.9 Microscope images of 2 wt% kaolinite suspension in the absence and presence of PCE (0.03 wt%) at pH=3.4 (a) and (b), and at pH=8.3 (c) and (d).

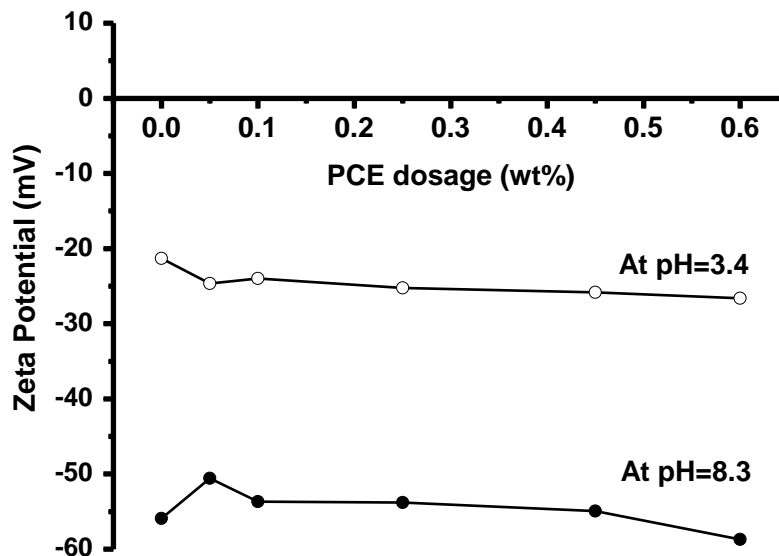


Figure 0.10 Zeta potential of 2 wt% kaolinite suspension with different PCE dosages.

Surface Forces measurement using SFA

In order to elucidate the role of PCE in kaolinite suspension, the normal forces between two model clay surfaces (mica with similar surface composition as kaolinite) were measured by an SFA in PCE solution of different concentrations. The normalized force-distance profiles measured at pH=3.4 and 8.3 are shown in Figure 0.11a and b respectively. The two mica surfaces were first brought close to reach a “hard wall”, and then followed by separation of the surfaces. The “hard wall” distance is defined as the mica-mica separation distance or thickness of confined polymers, which does not appear to change with the increase of the normal compressive load or pressure.

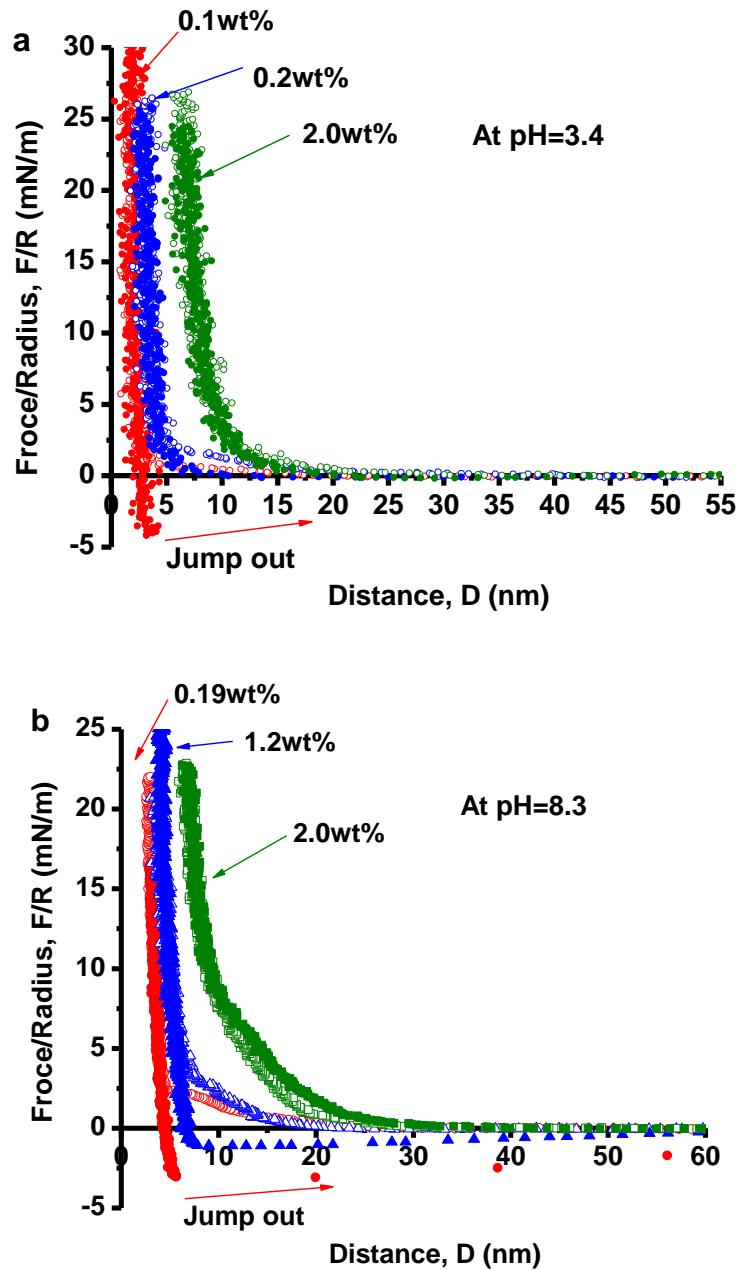


Figure 0.11 Force-distance profiles between two mica surfaces in different concentrations of PCE solution both at pH=3.4 (a) and pH=8.3 (b). Open symbols represent approach and filled symbols represent separation.

As shown in Figure 0.11a, at pH=3.4, an adhesion $F_{ad}/R \sim -4$ mN/m was measured between two mica surfaces in 0.1 wt% PCE solution which corresponds

to a PCE dosage of 0.27 wt%, where the suspension viscosity reaches the maximum in the viscosity measurement. In the viscosity measurement, 0.27 wt% was the polymer/kaolinite mass ratio. This polymer/kaolinite mass ratio was converted to the polymer/suspension mass ratio by: concentration of PCE in suspension% = 35 wt% (concentration of kaolinite suspension or kaolinite/suspension mass ratio) \times 0.27 wt% = 0.0945 % \approx 0.1 wt%. Similar conversion was done for the case at pH=8.3. As the PCE concentration increased to 0.2 wt% or above, only pure repulsive force were observed. The hard wall distances shifted from 2, 3 to 7 nm as the PCE concentrations increased from 0.1 wt%, 0.2 wt% to 2.0 wt%, respectively.

From Figure 0.11b, at pH=8.3, an adhesion $F_{ad}/R \sim -4$ mN/m was also measured during the separation of two mica surfaces in PCE solution of the lowest concentration investigated 0.19 wt% which corresponds to 0.54 wt% of PCE dosage in the viscosity measurement, and the hard wall distance was ~ 2 nm. The adhesion decreased to $F_{ad}/R \sim -1$ mN/m as the PCE concentration increased to 1.2 wt% (corresponding to a PCE dosage of 3.2 wt% in the viscosity measurement), and the hard wall distance shifted to ~ 4 nm. With the PCE concentration further increased to 2.0 wt%, only pure repulsive force was observed and the hard wall distance shifted to ~ 7 nm.

For both acidic and alkaline conditions, adhesion was observed in PCE solutions of low concentration (0.1 wt% at pH=3.4 and 0.19 wt% at pH=8.3), which was mainly caused by the bridging attraction of the PCE molecules confined between the two mica surfaces through hydrogen bonding. Interestingly,

the maximum viscosity of PCE solution was observed at the same PCE concentration (dosages of ~ 0.27 wt% and ~ 0.54 wt% for pH=3.4 and 8.3 respectively) as shown in Figure 0.3e and f, which indicates that the bridging adhesion between clay surfaces by PCE enhanced the viscosity of clay suspension, but much more significantly for the alkaline solution at pH=8.3.

At pH=3.4, as the PCE concentration increased to 0.2 wt% or above, no bridging adhesion was measured, in consistent with the viscosity measurement shown in Figure 0.3e that the viscosity of kaolinite suspension with the same PCE dosage at pH=3.4 dropped back to or even slightly below the initial suspension viscosity without PCE. The increased hard distance at high PCE concentration indicates that the excess PCE molecules in the suspension induced strong steric repulsion between clay particles or small aggregates. The surface force measurements in Figure 0.11a, together with the viscosity results shown in Figure 0.3a, Figure 0.3c and Figure 0.3e for kaolinite suspensions under acidic condition, indicate that the high viscosity of kaolinite suspension at pH=3.4 is mainly due to the presence of clay aggregates and determined by the strong electrostatic interaction between negatively charged clay basal planes and positively charged edge surfaces, while the presence of PCE molecules and their interaction with clay particles have relatively weak impact on the suspension viscosity.

Under alkaline condition (pH=8.3), PCE molecules are fully stretched in aqueous solution and show the comb-shape configuration. The extended PEO side chains are able to form hydrogen bonding with clay surfaces and other PEO chains of other PCE molecules, which is evident by the bridging adhesion

measured between mica surfaces at low PCE concentrations (≤ 1.2 wt%) shown in Figure 0.11b. As mica has similar surface composition as kaolinite, PCE can bridge the kaolinite particles in the suspension at pH=8.3 when the solid particles are concentrated enough and the PCE concentration is not too high. The strong bridging attraction makes the kaolinite particles and PCE suspension form a strong “network” together with the associated water, leading to the high viscosity measured for concentrated kaolinite suspension (35 wt%) in the presence of PCE of low dosages shown in Figure 0.3f. The concentrated kaolinite suspension ensures that the particle separation is close enough so the PCE molecules are able to induce the attractive bridging force. Such a dramatic increase of viscosity was not observed for kaolinite suspension of lower clay concentrations (10 wt% and 2 wt%) as shown in Figure S0.1 in the Supplementary Information. At pH=8.3, as the concentration of PCE solution increases, the surface coverage of PCE polymer on both mica surfaces increases, and the intermolecular hydrogen bonding among the PCE molecules also increases. The comb-shaped PCE molecules adsorbed on mica act as polymer brushes, leading to strong steric repulsion when the two mica surfaces approach each other, which is evident by the relatively longer range of repulsion during the approaching force-distance profiles shown in Figure 0.11b than that measured at pH 3.4 in Figure 0.11a. As a result, at high PCE concentration, the steric repulsion arisen from the absorbed PCE and the PCE molecules in the solution prevents the formation of inter-locked kaolinite-PCE “network”, and the highly hydrated comb-shaped PCE act further as a lubricant

between the clay particles, which leads to a dramatic decrease of the suspension viscosity.

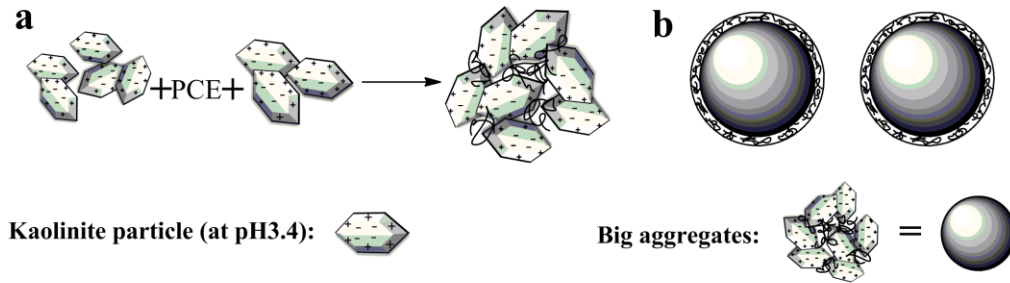
Schematic model of interactions between PCE and kaolinite particles

Based on the above results via the various techniques including viscosity measurement, microscopic imaging, settling tests, zeta potential and surface forces measurement, a schematic model for the interactions between PCE molecules and kaolinite particles is proposed in Figure 0.12. Figure 0.12a shows that at pH=3.4 kaolinite clay particles can self-aggregate through the electrostatic attraction between negatively charged clay basal planes and positively charged edge surfaces, and a low dosage of PCE can bring small aggregates together via the hydrogen bonding between PEO side chains and clay surfaces. At higher dosages, PCE molecules can fully cover the self-aggregated clay particles (Figure 0.12b) and induce strong steric repulsion between these aggregates.

At pH=8.3 and low PCE dosage, PCE polymer can bridge the kaolinite particles together as long as the distance between clay particles and polymer is close enough, as shown in the schematic of Figure 0.12c. Under alkaline condition, the PCE polymer is fully stretched and comb-shaped due to the repulsive force between negatively charged carboxylate groups on the backbone and steric interactions between highly hydrated PEO side chains. Therefore, for concentrated kaolinite suspension under alkaline condition, PCE molecules are able to bind particles together and form a strong network via hydrogen bonding between PCE molecules and particle surfaces, which significantly enhances the suspension viscosity by over 100 times. At high PCE dosages, the PCE molecules

fully cover the clay particle surfaces, inducing strong steric repulsive forces among the particles as shown in the schematic of Figure 0.12d and dramatically decreasing the suspension viscosity.

Acidic condition



Alkaline condition

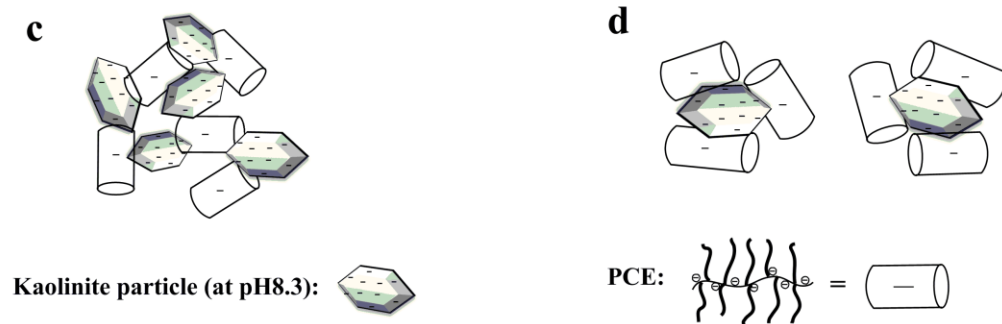


Figure 0.12 Illustrations on the interactions between kaolinite particles and PCE molecules at acidic condition (pH=3.4) (a) & (b), and at alkaline condition (pH=8.3) (c) & (d): (a) pH=3.4 with low PCE dosage; (b) pH=3.4 with high PCE dosage; (c) pH=8.3 with low PCE dosage; (d) pH=8.3 with high PCE dosage.

1.19 Conclusion

The viscosity and interfacial properties of kaolinite clay particles and the impact of a polycarboxylate ether comb-type polymer was determined at both acidic and alkaline pHs. Solution pH, concentration of clay particles and PCE dosage (weight percentage of the particles) all play important roles in the

viscosity and interfacial properties of the clay suspension. For 35 wt% kaolinite suspension without PCE polymer, the viscosity of clay suspension in acidic condition (pH=3.4) is over 100 times higher than that in alkaline condition (pH=8.3). At pH=3.4, the addition of PCE comb-type polymer did not significantly affect the viscosity of kaolinite suspension, but at pH=8.3 it dramatically enhanced the suspension viscosity by over 100 times at low PCE dosage (≤ 0.6 wt%) and then decreased the suspension viscosity back to original value when further increasing the PCE dosage (≥ 3 wt%). PCE comb-type polymer was shown to be a good dispersant for kaolinite suspension under alkaline condition for almost all PCE dosages, and no obvious settling or particle aggregation was observed. However under acidic condition, the PCE acts as a good dispersant only at relatively high dosage (e.g., ≥ 0.4 wt%). For suspensions with low solid clay content (10 wt% and 2 wt%), the PCE comb-type polymer showed much weaker impact on the viscosity of clay suspension (see the effects of solid content in the Supplementary Information).

The impact of pH and presence of PCE polymer on the viscosity of clay suspension and its interfacial properties was further elucidated by determining the intermolecular and surface interactions among the clay particles and PCE molecules. Under acidic condition, the high viscosity of kaolinite suspension was mainly attributed to the electrostatic attraction between negatively charged basal planes and positively edge surfaces. For highly concentrated clay suspension, as the particles were close to certain critical distance the PCE molecules could induce attractive bridging interaction via hydrogen bonding between clay

particles, leading the clay particles and PCE polymer to form a strong “network” and thus dramatically increasing the suspension viscosity under alkaline condition. At high PCE dosages, the steric repulsion force between the PCE molecules absorbed on clay particles dominates the particle interactions, decreasing the viscosity of clay suspension and forming a stable clay-polymer suspension. The viscosity and interfacial properties obtained in the present study on kaolinite suspension with comb-type PCE polymer provide an insight into the fundamental interactions between clay/colloidal particles and polymer additives in many engineering applications and industrial processes.

Supplementary Information

Effects of solid content

Compared with the 35 wt% case, the viscosity of 10 wt% and 2 wt% kaolinite suspension in the presence of PCE at pH=8.3 was measured and shown in Figure S0.1. Figure S0.1 indicates that although the viscosity change with the addition of PCE of different concentration showed similar trend with that of 35 wt% kaolinite suspension, the viscosity increment was much smaller. For the 2 wt% of kaolinite suspension, there was almost no obvious change in viscosity within the whole range of PCE dosages used. Therefore, the solid content of suspension also plays an important role in the interactions between kaolinite particles and PCE.

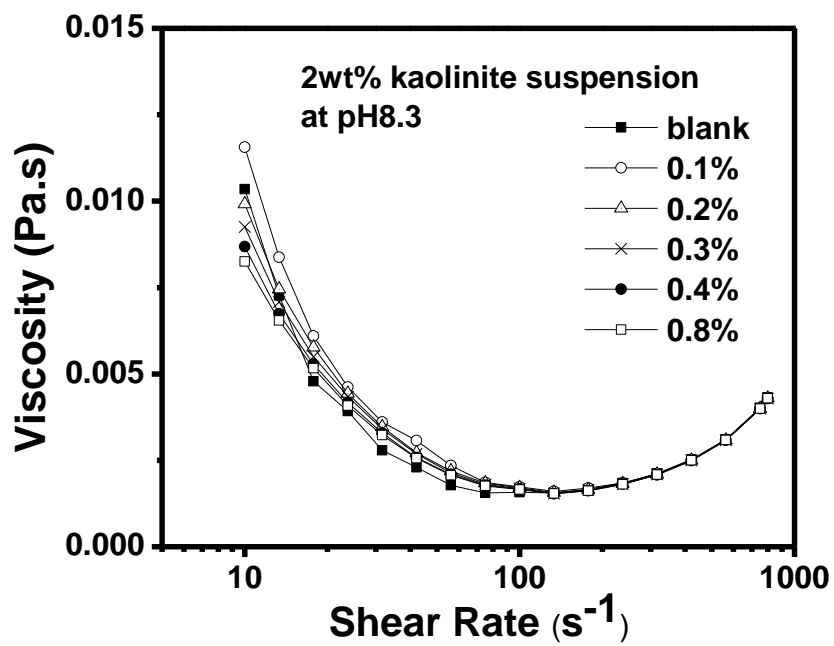
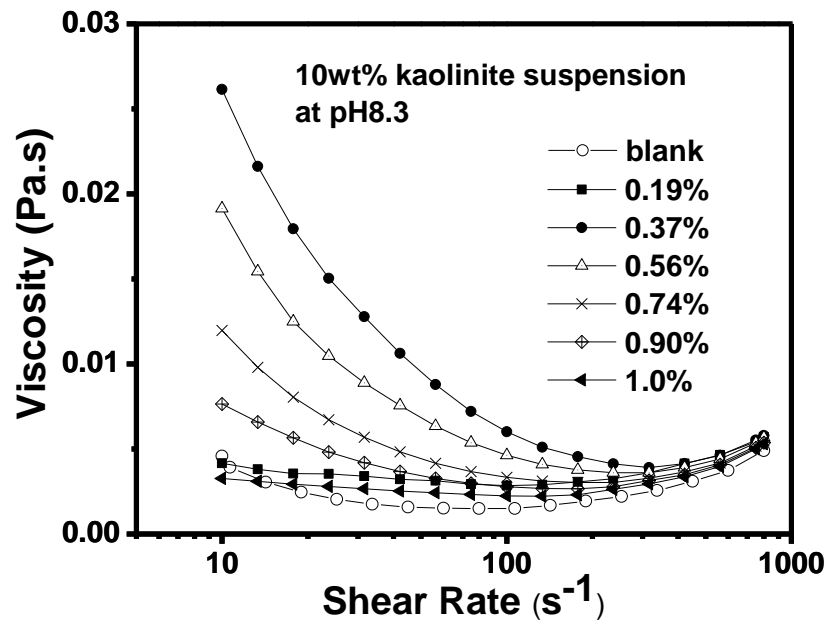


Figure S0.1 Effect of different PCE dosages on the viscosity of 10 wt% and 2 wt% kaolinite suspension at pH=8.3.

References

- [1] M.E. Holuszko, J.S. Laskowski, *Coal Prep*, 24 (2004) 179.
- [2] D. Tao, X.H. Zhou, D. Kennedy, P. Dopico, J. Hines, *Sep Sci Technol*, 45 (2010) 604.
- [3] D. Tao, G.L. Chen, X.H. Zhou, C. Zhao, M.M. Fan, M. Aron, J. Wright, *Can Metall Quart*, 46 (2007) 243.
- [4] O.B. Adeyinka, S. Samiei, Z.H. Xu, J.H. Masliyah, *Can J Chem Eng*, 87 (2009) 422.
- [5] S.H. Chang, R.K. Gupta, M.E. Ryan, *J Rheol*, 36 (1992) 273.
- [6] P. Mporu, J. Addai-Mensah, J. Ralston, *Int J Miner Process*, 71 (2003) 247.
- [7] M.L. Taylor, G.E. Morris, P.G. Self, R.S. Smart, *J Colloid Interf Sci*, 250 (2002) 28.
- [8] J. Long, H. Li, Z. Xu, J.H. Masliyah, *Aiche J*, 52 (2006) 371.
- [9] M. Sjoberg, L. Bergstrom, A. Larsson, E. Sjostrom, *Colloid Surface A*, 159 (1999) 197.
- [10] V.S. Ramachandran, *Cement Concrete Comp*, 20 (1998) 149.
- [11] K. Yoshioka, E. Sakai, M. Daimon, A. Kitahara, *J Am Ceram Soc*, 80 (1997) 2667.
- [12] K.L. Konan, C. Peyratout, M. Cerbelaud, A. Smith, J.P. Bonnet, A. Jacquet, *Appl Clay Sci*, 42 (2008) 252.
- [13] W.Y. Yang, J.W. Qian, Z.Q. Shen, *J Colloid Interf Sci*, 273 (2004) 400.

- [14] J. Long, Z. Xu, J.H. Masliyah, *Energ Fuel*, 19 (2005) 1440.
- [15] P. Mporu, J. Addai-Mensah, J. Ralston, *J Colloid Interf Sci*, 271 (2004) 145.
- [16] A. McFarlane, K. Bremmell, J. Addai-Mensah, *J Colloid Interf Sci*, 293 (2006) 116.
- [17] H. Xiao, Z. Liu, N. Wiseman, *J Colloid Interf Sci*, 216 (1999) 409.
- [18] C.P. Whitby, P.J. Scales, F. Grieser, T.W. Healy, G. Kirby, J.A. Lewis, C.F. Zukoski, *J Colloid Interf Sci*, 262 (2003) 274.
- [19] C. Li, X. Yu, P. Somasundaran, *Colloid Surface*, 66 (1992) 39.
- [20] M. Kinoshita, Y. Yuki, K. Saitou, T. Takahashi, *Kobunshi Ronbunshu*, 52 (1995) 357.
- [21] R.J. Flatt, I. Schober, E. Raphael, C. Plassard, E. Lesniewska, *Langmuir*, 25 (2009) 845.
- [22] L. Ferrari, J. Kaufmann, F. Winnefeld, J. Plank, *J Colloid Interf Sci*, 347 (2010) 15.
- [23] A. Zingg, F. Winnefeld, L. Holzer, J. Pakusch, S. Becker, R. Figi, L. Gauckler, *Cement Concrete Comp*, 31 (2009) 153.
- [24] A. Kauppi, K.A. Andersson, L. Bergstrom, *Cement Concrete Res*, 35 (2005) 133.
- [25] F. Winnefeld, S. Becker, J. Pakusch, T. Gotz, *Cement Concrete Comp*, 29 (2007) 251.

- [26] A. Zingg, F. Winnefeld, L. Holzer, J. Pakusch, S. Becker, L. Gauckler, J Colloid Interf Sci, 323 (2008) 301.
- [27] J. Long, Z.H. Xu, J.H. Masliyah, Langmuir, 22 (2006) 1652.
- [28] A.R. Al-Hashmi, P.F. Luckham, Colloid Surface A, 358 (2010) 142.
- [29] W. Sun, J. Long, Z.H. Xu, J.H. Masliyah, Langmuir, 24 (2008) 14015.
- [30] H. Haschke, M.J. Miles, V. Koutsos, Macromolecules, 37 (2004) 3799.
- [31] U. Raviv, S. Giasson, N. Kampf, J.F. Gohy, R. Jerome, J. Klein, Langmuir, 24 (2008) 8678.
- [32] N. Kampf, J.F. Gohy, R. Jerome, J. Klein, J Polym Sci Pol Phys, 43 (2005) 193.
- [33] P.F. Luckham, J. Klein, J Chem Soc Faraday T, 86 (1990) 1363.
- [34] M.A. Bevan, D.C. Prieve, Langmuir, 16 (2000) 9274.
- [35] S. Biggs, Langmuir, 11 (1995) 156.
- [36] J. Israelachvili, Intermolecular and Surface Forces, third ed., Academic Press, 2011.
- [37] J. Israelachvili, Y. Min, M. Akbulut, A. Alig, G. Carver, W. Greene, K. Kristiansen, E. Meyer, N. Pesika, K. Rosenberg, H. Zeng, Rep Prog Phys, 73 (2010) 1.
- [38] A. Natarajan, J.G. Xie, S.Q. Wang, Q.X. Liu, J. Masliyah, H.B. Zeng, Z.H. Xu, J Phys Chem C, 115 (2011) 16043.
- [39] F.C. Teng, H.B. Zeng, Q.X. Liu, J Phys Chem C, 115 (2011) 17485.

- [40] Q.Y. Lu, J. Wang, A. Faghijnejad, H.B. Zeng, Y. Liu, *Soft Matter*, 7 (2011) 9366.
- [41] Israelac.Jn, *J Colloid Interf Sci*, 44 (1973) 259.
- [42] B. Rand, I.E. Melton, *J Colloid Interf Sci*, 60 (1977) 308.
- [43] H. van Olphen, *Introduction to Clay Colloid*, Interscience (Wiley), New York, 1963.
- [44] V. Gupta, J.D. Miller, *J Colloid Interf Sci*, 344 (2010) 362.
- [45] W.J. Tseng, C.H. Wu, *Acta Mater*, 50 (2002) 3757.
- [46] A.R. Studart, E. Amstad, M. Antoni, L.J. Gauckler, *J Am Ceram Soc*, 89 (2006) 2418.
- [47] E. Pefferkorn, L. Nabzar, A. Carroy, *J Colloid Interf Sci*, 106 (1985) 94.
- [48] E. Pefferkorn, L. Nabzar, R. Varoqui, *Colloid Polym Sci*, 265 (1987) 889.
- [49] F.F. Peng, P.K. Di, *J Colloid Interf Sci*, 164 (1994) 229.
- [50] H. Hommer, *J Eur Ceram Soc*, 29 (2009) 1847.
- [51] L.M. Vane, G.M. Zang, *J Hazard Mater*, 55 (1997) 1.
- [52] Y. Yukselen, A. Kaya, *Water Air Soil Poll*, 145 (2003) 155.
- [53] F. Nsib, N. Ayed, Y. Chevalier, *Colloid Surface A*, 286 (2006) 17.

CHAPTER 5 SUMMARY

The molecular interactions of two comb-type polymers PS-g-PEO and PCE have been investigated at air/water/solid interfaces, both of which have the same grafted side chains (polyethylene oxide). From the above studies, it was found that the two comb-type polymers show completely different interfacial properties and molecular interactions in aqueous solutions.

For comb-type polymer PS-g-PEO, only pure repulsive forces were detected in both symmetric (polymer vs. polymer) and asymmetric configurations (polymer vs. mica) in NaCl solutions and all the forces detected were independent on the ionic strength of NaCl solution due to the neutral nature of PEO branches. The long-range repulsive forces were attributed to the steric hindrance arising from the interactions of neutral swollen PEO brushes in aqueous solutions which was supported by the well fitted forces curves using Alexander-de Gennes scaling theory. The contact angle measurement provided evidence that the PEO branch chains can rearrange their conformations and extend into the aqueous solution due to the strong van de Waals force and hydrogen bonding between hydrophilic PEO segments and water molecules.

The polycarboxylate ether (PCE) comb-type polymer shows great impact on the concentrated kaolinite suspension and the interaction forces of PCE solutions between two mica surfaces (modelled clay surfaces) were completely different with the first case. Solution pH, concentration of clay particles and PCE dosage (weight percentage of the particles) all play important roles in the viscosity and

interfacial properties of the clay suspension. At pH=3.4, the addition of PCE comb polymer did not significantly affect the viscosity of kaolinite suspension, but at pH=8.3 it dramatically enhanced the suspension viscosity by over 100 times at low PCE dosage (≤ 0.6 wt%) and then decreased the suspension viscosity back to original value when further increasing the PCE dosage (≥ 3 wt%). For suspensions with low solid clay content (10 wt% and 2 wt%), the PCE comb polymer showed much weaker impact on the viscosity of clay suspension. Combined with the results of surface force measurement, it is elucidated that at lower PCE dosages, the high viscosity of kaolinite suspension was mainly attributed to the electrostatic attraction between negatively charged basal planes and positively edge surfaces under acidic condition. However, under alkaline condition, as the particles were close to certain critical distance in highly concentrated clay suspension, the PCE molecules could induce attractive bridging interaction via hydrogen bonding between clay particles, leading the clay particles and PCE polymer to form a strong “network” and thus dramatically increasing the suspension viscosity. At high PCE dosages, the steric repulsion force between the PCE molecules absorbed on clay particles dominates the particle interactions, decreasing the viscosity of clay suspension and forming a stable clay-polymer suspension.

Previous reports have shown that polyethylene oxide (PEO) homopolymer, and its grafted polymers and copolymers (di-block and tri-block) have a wide range of applications. [1-5] This thesis work suggests that comb-type PS-g-PEO and PCE and their derivatives may also have important engineering applications

(e.g., in mineral processing), which will be further investigated in future work. The above research further implies that the properties of comb-type polymers may be manipulated in terms of functional groups on the backbone and side chains, length and density of side chains, and the chemical composition of side chains (homopolymer or copolymer) for different applications. The results in this thesis provide important insights into fundamental understanding of molecular interaction mechanisms of comb-type polymers at air/water/solid interfaces and the development of novel functional polymers/coatings for engineering and biomedical applications.

References

- [1] M.V. Smalley, H.L.M. Hatharasinghe, I. Osborne, J. Swenson, S.M. King, *Langmuir*, 17 (2001) 3800.
- [2] P. Mporu, J. Addai-Mensah, J. Ralston, *Int J Miner Process*, 71 (2003) 247.
- [3] C.P. Whitby, P.J. Scales, F. Grieser, T.W. Healy, G. Kirby, J.A. Lewis, C.F. Zukoski, *J Colloid Interf Sci*, 262 (2003) 274.
- [4] P. Mporu, J. Addai-Mensah, J. Ralston, *J Colloid Interf Sci*, 271 (2004) 145.
- [5] Q.P. Ran, P. Somasundaran, C.W. Miao, J.P. Liu, S.S. Wu, J. Shen, *J Colloid Interf Sci*, 336 (2009) 624.